

## The S<sup>4</sup>G-WISE View of Global Star Formation in the Nearby Universe

M.E. CLUVER <sup>1,2</sup> T.H. JARRETT <sup>3,4,1</sup> D.A. DALE <sup>5</sup> J.-D.T. SMITH <sup>6</sup> M.J.I. BROWN <sup>7</sup> W. VAN KEMPEN <sup>1</sup>  
E. LENGNERER <sup>1</sup> R. INCOLL <sup>1</sup> C. DAVEY <sup>1</sup> R. HOLLOWAY <sup>1</sup> J. CAMERON <sup>1</sup> AND K. SHETH <sup>8</sup>

<sup>1</sup>Centre for Astrophysics and Supercomputing, Swinburne University of Technology, John Street, Hawthorn, 3122, Australia

<sup>2</sup>Department of Physics and Astronomy, University of the Western Cape, Robert Sobukwe Road, Bellville, 7535, South Africa

<sup>3</sup>Institute for Astronomy, University of Hawaii at Hilo, 640 N Aohoku Pl 209, Hilo, HI 96720, USA

<sup>4</sup>Department of Astronomy, University of Cape Town, Rondebosch, South Africa

<sup>5</sup>Department of Physics and Astronomy, University of Wyoming, Laramie, WY 82071, USA

<sup>6</sup>Ritter Astrophysical Research Center, University of Toledo, Toledo, OH 43606, USA

<sup>7</sup>School of Physics and Astronomy, Monash University, Clayton 3800, VIC, Australia

<sup>8</sup>NASA Headquarters, 300 Hidden Figures Way SW, Washington, D.C.

(Accepted 17 October 2024)

Submitted to ApJ

### ABSTRACT

In this work we present source-tailored *WISE* mid-infrared photometry (at 3.4  $\mu\text{m}$ , 4.6  $\mu\text{m}$ , 12  $\mu\text{m}$ , and 23  $\mu\text{m}$ ) of 2812 galaxies in the extended *Spitzer* Survey of Stellar Structure in Galaxies (S<sup>4</sup>G) sample, and characterise the mid-infrared colors and dust properties of this legacy nearby galaxy data set. Informed by the relative emission between W3 (12  $\mu\text{m}$ ) and W4 (23  $\mu\text{m}$ ), we re-derive star formation rate (SFR) scaling relations calibrated to  $L_{\text{TIR}}$ , which results in improved agreement between the two tracers. By inverse-variance weighting the W3 and W4-derived SFRs, we generate a combined mid-infrared SFR that is a broadly robust measure of star formation activity in dusty, star-forming galaxies in the nearby Universe. In addition, we investigate the use of a W3-derived dust density metric,  $\Sigma_{12\mu\text{m}}$  ( $L_{\odot}/\text{kpc}^2$ ), to estimate the SFR deficit of low mass, low dust galaxies. This is achieved by combining *WISE* with existing GALEX ultraviolet (UV) photometry, which we further use to explore the relationship between dust and UV emission as a function of morphology. Finally, we use our derived SFR prescriptions to examine the location of galaxies in the  $\log \text{SFR} - \log M_{\text{stellar}}$  plane, as a function of morphological type, which underscores the complexity of dust-derived properties seen in galaxies of progressively earlier type.

*Keywords:* galaxies:general, galaxies:star formation, galaxies:photometry, infrared:galaxies

### 1. INTRODUCTION

The local Universe furnishes the benchmark that underpins our understanding of how galaxies have evolved over cosmic time. Here we can assemble a near complete view of a diverse zoo of galaxy specimens and, with homogeneous observations at multiple wavelengths, characterise the properties of different sub-populations of the nearby Universe.

One such benchmark sample is the *Spitzer* Survey of Stellar Structure in Galaxies (S<sup>4</sup>G; Sheth et al. 2010), created as a uniform legacy survey using the *Spitzer Space Telescope* and its ‘warm’ imaging bands (IRAC-1, 3.6  $\mu\text{m}$  and IRAC-2, 4.5  $\mu\text{m}$ ). S<sup>4</sup>G concentrated on the local volume within 40 Mpc, initially targeting  $\sim 2300$  galaxies of a wide variety of morphological types and stellar masses, but later expanded to over 2800 galaxies by including additional early-type systems. The survey was notably designed to study the stellar mass distribution of nearby galaxies since the 3.6  $\mu\text{m}$  and 4.5  $\mu\text{m}$  channels sensitively track the Rayleigh-Jeans tail of the stellar light distribution from luminous, evolved stars that

dominate the baryonic mass of normal, evolved galaxies (see studies by Muñoz-Mateos et al. 2013; Meidt et al. 2014; Querejeta et al. 2015).

These nearby sources can often be challenging to measure, not least because they are so large on the sky. But, equivalently, they provide the highest signal to noise measurements for both global and local (i.e. sub-galactic) studies of star formation (see Kennicutt & Evans 2012, and references within). Where studies of star formation on sub-kpc scales provide insight into the physics and chemistry of this key process (e.g. Sun et al. 2023; Calzetti et al. 2024; Peltonen et al. 2024), global measures of star formation rate (SFR) are a fundamental property of large, statistical studies of galaxy evolution, particularly in combination with stellar mass (e.g. Noeske et al. 2007; Whitaker et al. 2014; Popesso et al. 2019; Goovaerts et al. 2024).

Multi-band photometry in combination with spectral energy distribution (SED) fitting is a powerful tool to extract stellar masses, SFRs, and dust properties (e.g. da Cunha et al. 2008; Chevallard & Charlot 2016; Leja et al. 2017; Boquien et al. 2019; Robotham et al. 2020), although the treatment of dust and its associated attenuation is far from trivial (e.g. Salim & Narayanan 2020; Pacifici et al. 2023) requiring detailed radiative transfer modelling (e.g. De Looze et al. 2014; Viaene et al. 2017; Williams et al. 2019). However, the combination of GALEX (Martin et al. 2005) ultraviolet (UV) and *WISE* mid-infrared imaging, accounting for both unobscured and obscured star formation, has been shown to be a powerful hybrid SFR indicator in the nearby Universe (e.g. Salim et al. 2016; Davies et al. 2016; Leroy et al. 2019; Belfiore et al. 2023), building on the work of, for example, Kennicutt (1998), Hao et al. (2011), and Boquien et al. (2016). This is well-illustrated in, for example, studies of the gas consumption and fueling of star formation in the Local Universe (e.g. Saintonge et al. 2017).

Dust reprocesses the radiation from stars, but, for example, dust content, dust geometry, and the contributions from young versus evolved stellar populations will influence the resulting infrared spectrum (see Calzetti 2013, and references within). As shown in Cluver et al. (2017), the power of *WISE* as a tracer of star formation activity lies in the fact that the  $12\ \mu\text{m}$  and  $23\ \mu\text{m}$  dust emission bands are well-correlated to total infrared luminosity ( $L_{\text{TIR}}$ ; Dale & Helou 2002) where the particularly close correspondence of  $L_{12\ \mu\text{m}}$  and  $L_{\text{TIR}}$  was noted by Spinoglio et al. (1995) using the *Infrared Astronomy Satellite (IRAS)* and further examined by Takeuchi et al. (2005). Hence, where  $L_{\text{TIR}}$  is expected to be a reliable measure of star formation (i.e. in typical, dusty

star-forming galaxies), *WISE*  $12\ \mu\text{m}$  and  $23\ \mu\text{m}$  channels offer a stable measurement of recent star formation in the local Universe. However, it should be noted that at  $z \sim 0$ , the *WISE* W3 and W4 bands measure two quite different parts of a galaxy’s spectral energy distribution, with potentially complex provenance and hence dependencies. In addition, the limitations inherent in the use of a monochromatic star formation indicator should always be carefully considered and weighed against the convenience of *WISE*’s all-sky coverage which allows for a uniform measure of star formation particularly useful in large area studies (e.g. Cluver et al. 2020).

In this study, we present source-tailored mid-infrared measurements of the expanded S<sup>4</sup>G sample derived using imaging from the *WISE* survey (Wright et al. 2010). Although the *WISE*  $3.4\ \mu\text{m}$  (W1) and  $4.6\ \mu\text{m}$  (W2) bands (with  $\sim 6''$  resolution) do not offer any improvement on the *Spitzer* observations, the *WISE*  $12\ \mu\text{m}$  (W3) and  $23\ \mu\text{m}$  (W4) bands allow us to examine the dust properties uniformly across the sample due to its all-sky coverage. Based on the observed dust emission characteristics, we re-derive the star formation rate calibrations of Cluver et al. (2017), finding much closer agreement between the W3 and W4 tracers.

The S<sup>4</sup>G-*WISE* sample covers the entire spectrum of galaxies observed in the local Universe; this diversity in morphological type and stellar mass allows us to examine the strengths and weaknesses of *WISE* in support of large surveys. To this end, we introduce a dust density metric,  $\Sigma_{12\ \mu\text{m}}$  ( $L_{\odot}/\text{kpc}^2$ ), that can be used to estimate the deficit in dust-derived star formation rates for low mass, low dust galaxies.

The all-sky coverage of the *WISE* survey fortifies its relevance as an ongoing resource for  $z < 0.1$  science, particularly in the Southern Hemisphere where mega-projects such as LSST (Ivezić et al. 2019), 4MOST (de Jong et al. 2019), and the Square Kilometer Array will create a rich scientific landscape in the next decade, and beyond. The work presented here will be followed by a companion paper that will present the *WISE* photometry and derived quantities (using the scaling relations presented in this current work) for a sample of  $\sim 17,000$  galaxies selected from the 2MASS Redshift Survey (Huchra et al. 2012); this Ks brighter than 11th mag sample, plus the S<sup>4</sup>G data presented here, will comprise the brightest and highest signal to noise (S/N) mid-infrared sample possible.

Throughout this paper mid-IR refers to the “mid-infrared” wavelengths and all four *WISE* bands are considered to be in the mid-infrared. Monochromatic luminosities are defined as  $\nu L_{\nu}$ , i.e.  $L_{12\ \mu\text{m}} \equiv \nu L_{\nu}(12\ \mu\text{m})$ ,  $M_{\text{stellar}}$  is the global stellar mass for individual galax-

ies and likewise, SFR is the global star formation rate. The adopted cosmology is  $H_0 = 70 \text{ km s}^{-1} \text{ Mpc}^{-1}$ ,  $\Omega_M = 0.3$  and  $\Omega_\Lambda = 0.7$ , but as detailed in the following section, robust redshift-independent and bulk flow corrected distances are used where available. All magnitudes are in the Vega system (*WISE* photometric calibration described in Jarrett et al. 2011). All linear fits are performed using the Hyper-fit package (Robotham & Obreschkow 2015).

## 2. DATA

Targeting the sample of galaxies that form part of S<sup>4</sup>G (Sheth et al. 2010), the primary photometric and source characterization is drawn from the *WISE* Extended Source Catalogue (WXSC Jarrett et al. 2013). The sample and data are described below.

### 2.1. The S<sup>4</sup>G Sample

S<sup>4</sup>G was a legacy program conducted as part of the *Spitzer* Space Telescope’s post-cryogenic mission which performed imaging of 2331 galaxies using the Infrared Array Camera (IRAC) 3.6  $\mu\text{m}$  and 4.5  $\mu\text{m}$  bands providing a volume-, magnitude- and size-limited sample (Sheth et al. 2010) to a distance of 40 Mpc.

The original S<sup>4</sup>G sample selection, however, suffered from a bias that notably excluded early-type galaxies. This was subsequently rectified by introducing a second sample,  $\sim 500$  galaxies, using morphology and distance information to sweep up any early type (bulge-dominated) galaxies within the volume. This latter sample is referred to as the S<sup>4</sup>G-ETG; details are provided in Watkins et al. (2022). We have combined the ‘classic’ sample with the ETG sample and measured their *WISE* counterparts to create the S<sup>4</sup>G-*WISE* sample consisting of 2812 galaxies. S<sup>4</sup>G galaxies are typically bright and well-resolved in the *WISE* imaging which allows us to relate morphological and structural characteristics to *WISE*-derived physical properties of stellar mass and star formation rate.

The S<sup>4</sup>G sample comes with meta-information including distance information and morphological classifications. However, instead of using the published distances in the earlier S<sup>4</sup>G catalogs, we make use of the latest distance information where available, notably taking advantage of redshift-independent compilations (NED-D V17.1.0) from the NASA Extragalactic Database (NED)<sup>1</sup>. We derive the distances in the following way: (1) if the source has a high quality (at least 3 independent measurements) mean redshift-independent distance, it is adopted, but if not, (2) search for the

source in the CosmicFlows-3 catalogue of galaxy distances (Tully et al. 2016), otherwise (3) we use the redshift to compute the luminosity distance after correcting to the CMB frame of reference (with  $H_0 = 70 \text{ km s}^{-1} \text{ Mpc}^{-1}$ ,  $\Omega_M = 0.3$ ). The majority of sources, 1525 ( $\sim 54\%$ ) have redshift-independent distances, a fraction of which have the highest quality distances from either Cepheid, Planetary Nebula Luminosity Function or Tip of the Red Giant Branch calibrations. Of these, 1174 come from CosmicFlows-3. The remainder of sources (1287) use distances derived from redshifts. Consequently, we can expect the best quality luminosities from the majority of the sample.

The sources are distributed across the sky, as shown in Fig. 1a, depicting the locations in Galactic projection. The plane of the Milky Way is completely avoided, removing any uncertainties from extinction and crowd confusion. The SuperGalactic Plane, dominated by the Virgo Cluster, is readily apparent in the sky distribution.

The distribution of distances in the S<sup>4</sup>G-*WISE* sample is shown in the histogram of Fig. 1b. The vast majority of galaxies are within 50 Mpc, consistent with the original 40 Mpc selection of S4G, but with a handful of sources (13) beyond 60 Mpc. The peak at  $\sim 20$  Mpc is the Virgo Supercluster. We note that several Local Group Galaxies,  $D < 1$  Mpc, are within the sample, including Andromeda (M31) and Triangulum (M33), and several low mass dwarfs that *WISE* was able to detect and characterize due to their close proximity (e.g., ESO 540-031). At the other extreme, the sample includes starburst galaxies (e.g., NGC 253 and M 82) and powerful AGN (NGC 1068) and other famous galaxies (e.g., M 101). Most of the sample would be classified as “normal” and hence, all in all, the S<sup>4</sup>G sample well-represents the zoo of galaxy types that comprise our local Universe.

### 2.2. *WISE* Imaging and Measurements

For over a decade we have made a concerted effort to identify, extract and characterize resolved galaxies imaged by *WISE*, building a rich database from which to draw catalogs. Preliminary catalog releases of the *WISE* Extended Source Catalogue (WXSC; Jarrett et al. 2013, 2019) describe the basic characterization methods, catalog features, and science results with the largest (angular size) galaxies in the sky. A much larger and more comprehensive subset of the WXSC will be released following this current work (Jarrett et al., in preparation). Here we briefly summarize the salient information relevant to this study.

<sup>1</sup> <https://ned.ipac.caltech.edu/Library/Distances/>

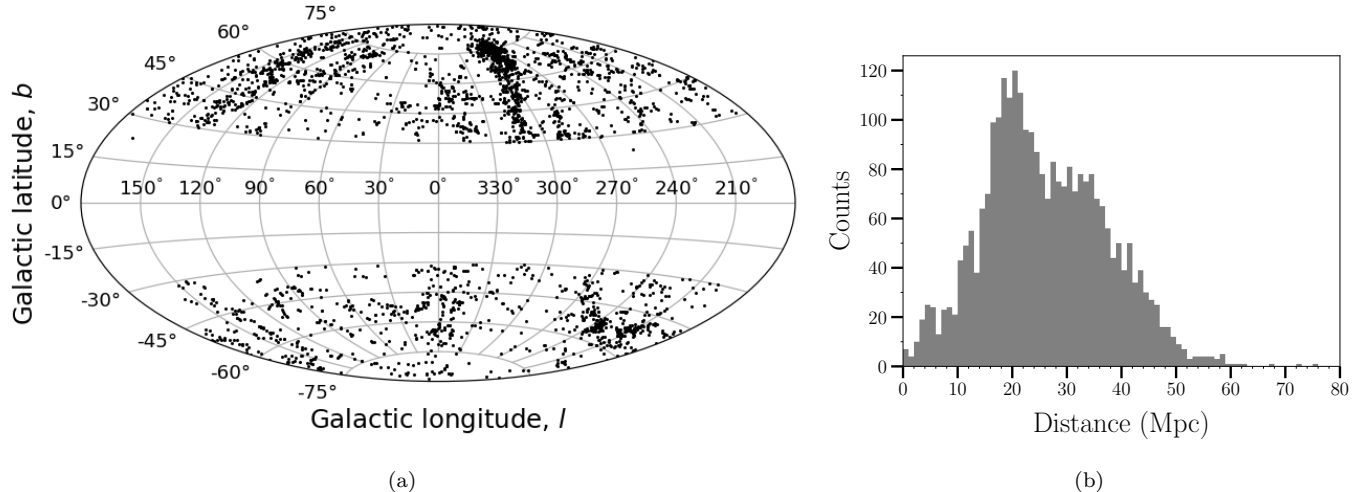


**Figure 1.** (a) Galactic Projection on-sky distribution of the  $S^4G$ -*WISE* sample (2812 galaxies). The Virgo Cluster gives rise to the overdensity in the North at  $\sim l = 280$  deg and the Fornax-Eridanus structure in the South at  $\sim l = 240$  deg. (b) The distance distribution of sources shows that the majority of galaxies lie within 50 Mpc.

Relative to the archival imaging and catalogs from the *WISE* project (e.g., ALLWISE catalog Cutri et al. 2012), the WXSC endeavors to: (1) improve upon 4-band image co-addition (mosaics), using custom mosaic construction (Jarrett et al. 2012) that includes the latest NEOWISE imaging and hence increases the sensitivity in the W1 and W2 bands, and (2) full source characterization that the diversity of galaxies demand, ranging from large, bright and massive galaxies to faint low surface brightness dwarfs. The W1 image mosaics reach 1-sigma depths (typically) fainter than  $23 \text{ mag arcsec}^{-2}$  ( $25.7 \text{ mag arcsec}^{-2}$  in AB mags), while native angular resolution ( $6''$  in W1) is preserved in all four bands. We note that with axi-symmetry, the radial surface profiles reach W1 depths of 25 to 26  $\text{mag arcsec}^{-2}$  ( $27.7 - 28.7 \text{ mag arcsec}^{-2}$  in AB mags), similar depths as to those of *Spitzer*-IRAC.

It is non-trivial to measure the properties of resolved galaxies, and hence the WXSC characterization pipeline has evolved over time (originating with 2MASS; Jarrett et al. 2003) to accommodate the *WISE* imaging strengths and limitations. As such, for the target galaxy, basic source characterization consists of five primary steps: (1) identify and remove foreground stars and local/background galaxies, a critical step since the beam is large and source blending is a significant challenge (see e.g., the method for de-blending galaxy pairs in Appendix B of Bok et al. 2020), (2) local “sky” background estimation, (3) fixed  $3\text{-}\sigma$  elliptical shape and orientation metrics, (4)  $1\text{-}\sigma$  isophotal radial size and flux determination, (5) central surface brightness and radial profile fitting to separate bulge and disk components, derive

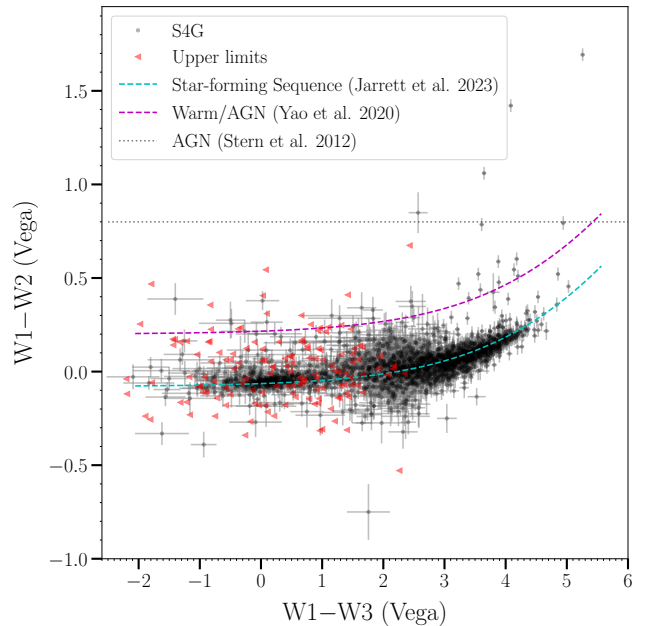


**Figure 2.** The Color Sequence: The *WISE* color-color plot for the  $S^4G$ -*WISE* sample shown as  $W1-W2$  versus  $W1-W3$ , including the star-forming sequence from Jarrett et al. (2023). The x-axis tracks the star formation history, from stellar-dominated to SF-dominated phases. Elevated  $W1-W2$  colors are a signature of dust heated by AGN; we include the relations of Stern et al. (2012) and Yao et al. (2020) above which the contribution of AGN activity should be taken into account.

total fluxes and concentration indices, and other miscellaneous characterization.

For well-resolved galaxies, axisymmetric radial profiles were constructed and fit with a double-Sérsic function designed to separate the spheroidal and disk population distributions, as well as extrapolate to larger radii to determine total fluxes down to several disk scale lengths. Further details can be found in Jarrett et al. (2013, 2019, 2023). Photometry measurements for the S<sup>4</sup>G sample are included in Table 1.

### 2.3. Derived Quantities

All fluxes and colors are rest-frame corrected using a large set of composite SED templates from Brown et al. (2014) and *Spitzer*-SWIRE/GRASIL (Polletta et al. 2006, 2007; Silva et al. 1998a) which span early-type spheroidals to late-type spirals, and include active Seyferts and AGNs of differing orientation types. Given the proximity of galaxies in S<sup>4</sup>G-WISE, the conversion to rest-frame properties (or “k-correction”) introduces a relatively small uncertainty, less than 3 to 4% (see also Jarrett et al. 2023). WISE is natively calibrated to Vega and all magnitudes are reported in this system (Wright et al. 2010; Jarrett et al. 2011).

The primary scaling parameters are the mid-IR luminosities. In the case of stellar mass, the in-band luminosity,  $L_{W1}$ , is the primary tracer of stellar mass (Jarrett et al. 2023). This luminosity is derived using

$$L_{W1}[L_{\odot}] = 10^{-0.4(M - M_{\text{SUN}})} \quad (1)$$

where  $M$  is the absolute magnitude of the source in W1 – determined from the W1 rest-frame flux, luminosity distance and the distance modulus – and 3.24 mag is the W1 in-band Solar value (Jarrett et al. 2013). All stellar masses in this paper are derived using the prescription outlined in Jarrett et al. (2023) which assumes a Chabrier (2003) IMF.

For measuring dust-obscured star formation we use the W3 and W4 spectral luminosities,  $\nu L_{\nu}(12 \mu\text{m})$  and  $\nu L_{\nu}(23 \mu\text{m})$ , after correcting for the contribution from the stellar continuum (using W1 as the proxy for the Rayleigh-Jeans model of the stellar emission, see Cluver et al. 2017; Jarrett et al. 2019). In this paper, we update the SFR relations of Cluver et al. (2017) using improved measurements, implementing more robust distance information, and correcting for low dust optical depths in dwarf galaxies; these details are in Section 3 and the Appendix.

Relevant to both  $M_{\text{stellar}}$  and SFR, the fundamental assumption is that W1 and W2 bands are tracing the Rayleigh-Jeans tail of the stellar light distribution. As discussed in Jarrett et al. (2013, 2019), we do not attempt to model or correct for any non-stellar emission in the W1 and W2 bands, such as the  $3.3 \mu\text{m}$  PAH feature, which is likely to be less than 10% for most normal

galaxies (e.g., see Lu et al. 2003). In a future study using JWST spectroscopy of the M51a galaxy, it will be possible to assess the impact of the  $3.3 - 3.4 \mu\text{m}$  PAH aliphatic feature – now easily detected in nearby galaxies using JWST (e.g., Lai et al. 2023) – on the integrated W1 emission for different SF environments.

Similarly, we do not attempt to account for any excess infrared emission in the mid-IR bands of W3 and W4, or the presence of silicate absorption. Hence for those cases where the WISE bands have significant AGB dust emission (old stars in the asymptotic giant branch phase), or AGN-accretion emission (e.g. ultraluminous infrared galaxies), the WISE luminosities may be contaminated and caution is recommended when interpreting the resulting  $M_{\text{stellar}}$  and SFR for extrema galaxies. Derived properties for the S<sup>4</sup>G-WISE sample are included in Table 2.

### 2.4. Morphologies

The proximity of galaxies in the S<sup>4</sup>G-WISE sample furnishes us with largely robust morphological information. We adopt the morphological classification methodology used in Bouquin et al. (2018), i.e. the RC2 classification scheme using numerical T-Types obtained from HyperLeda (Makarov, Dmitry et al. 2014). This is summarized here for convenience:  $-5 \leq E \leq -3.5$ ,  $-3.5 \leq E/S0 \leq -2.5$ ,  $-2.5 \leq S0 \leq -1.5$ ,  $-1.5 \leq S0/a \leq 0.5$ ,  $0.5 \leq Sa \leq 2.5$ ,  $2.5 \leq Sb \leq 4.5$ ,  $4.5 \leq Sc \leq 7.5$ ,  $7.5 \leq Sd \leq 8.5$ ,  $8.5 \leq Sm \leq 9.5$ , and  $9.5 \leq Irr \leq 999$ .

## 3. RESULTS

### 3.1. S<sup>4</sup>G-WISE: Colours and Mass by Morphological Type

Mid-IR colors are a simple, yet powerful diagnostic tool which can help inform sample selection and population studies. The WISE color-color diagram for the entire sample is shown in Figure 2; the star-forming sequence from Jarrett et al. (2023) – which roughly tracks star formation history through W1–W3 color, and excesses due to e.g. AGN through W1–W2 color – shows good agreement with the diverse S<sup>4</sup>G sample. Also shown is the AGN delineation from Stern et al. (2012); we find 8 galaxies with highly elevated W1–W2 colors, namely NGC 1068, NGC 3094, NGC 5506, UGC 04704, NGC 5253, NGC 4151, ESO 605-015, and NGC 4355. The latter has the most extreme WISE colours (W1–W3= 6.151 and W1–W2= 0.814 mag) and is beyond the limits of the axes shown in Figure 2.

Also shown is the “warm” line derived in Yao et al. (2020) above which sources likely have a component of AGN heating (based on optical emission line ratios). Elevated W1–W2 colors signal the presence of a hot dust

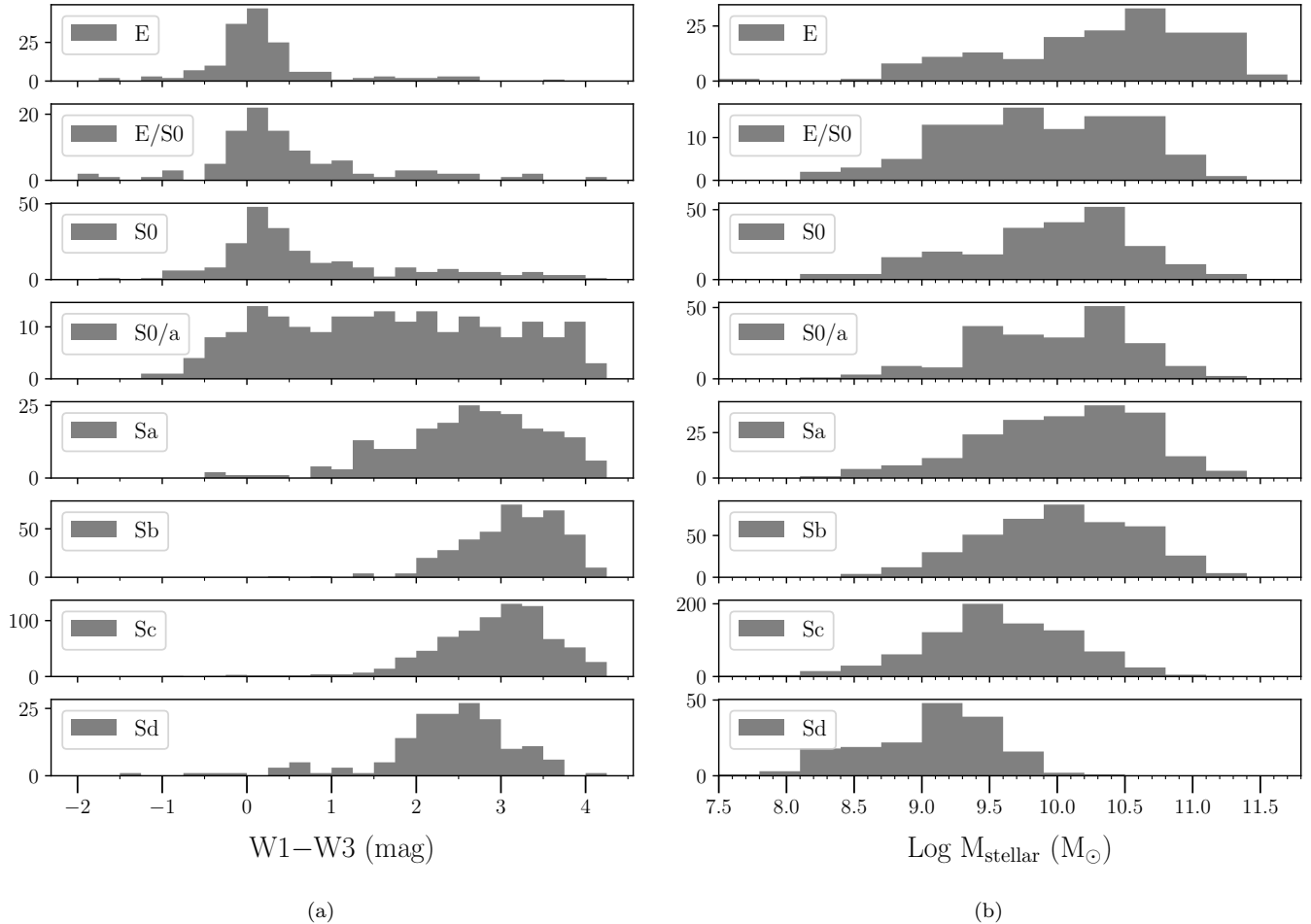


**Figure 3.** Galaxy Morphology Phase Space: (a) The W1–W3 colors separated by morphology illustrating the complexity of mapping color to galaxy type. (b) The stellar mass distribution for different morphological types within the S<sup>4</sup>G-*WISE* sample; we observe that a clear progression of stellar mass increasing as bulge prominence increases does not apply to all bulge-dominated systems (notably E and S0) which can be low mass.

component that will translate into an overestimation of stellar mass using the simple prescriptions we employ. This component will additionally boost the emission detected in the longer wavelength bands used to track star formation activity. We therefore exclude sources that lie above the Yao et al. (2020) line in the analysis that follows.

In Figure 3a we examine the W1–W3 color distribution as a function of morphological type (excluding sources with unreliable colors; W1–W3 error > 0.5 mag). This confirms that late-type (disk-dominated) galaxies tend to exhibit redder *WISE* colors compared to early-type (bulge-dominated) systems, with the clear exception being S0/Sa systems which occupy the full range of W1–W3 colors. The blueward shift of the Sd distribution compared to Sc is likely reflecting, on average, lower dust content paired with lower metallicity

in these systems. We do not present results for irregular morphological types due to the challenging nature of these measurements.

The relationship between stellar mass and morphological type is shown in Figure 3b; to select the most reliable sources we exclude those with a W1–W2 error > 0.2 mag (see Jarrett et al. 2023). As expected, we see a trend of disk-dominated galaxies occupying the lower mass regime, compared to high stellar mass systems that are more likely to be bulge-dominated. What is interesting is that early types (E to Sa) occupy a broad range in M<sub>stellar</sub>, and hence bulge-dominated systems are on average a poor predictor of stellar mass. Indeed, a number of S<sup>4</sup>G galaxies are classified as dwarf spheroidals, consistent with both their *WISE* color and derived stellar mass.

To better examine the relationship between *WISE* color and morphology we show the *normalised distribution* of a subset of sources extracted as follows using numerical T-Types:  $-5 \leq E \leq -3.5$ ,  $-2.5 \leq S0, S0/a \leq 0.5$ ,  $0.5 \leq Sa-Sb \leq 4.5$ ,  $4.5 \leq Sc-Sd \leq 8.5$ . Figure 4 underscores the broad range of mid-IR color that S0 and S0/a galaxies occupy, whereas disk galaxies appear to separate relatively cleanly from those classified as pure ellipticals.

### 3.2. The *WISE* Star Formation Bands at $z \sim 0$

We next examine the relationship between the W3 and W4 bands; the S<sup>4</sup>G-*WISE* sample is particularly powerful in this regard since nearby galaxies provide high quality  $12\ \mu\text{m}$  and  $23\ \mu\text{m}$  measurements usually lacking in more distant samples where the lower sensitivity of the W4 band precludes a high signal-to-noise comparison. Although both W3 and W4 trace dust, they measure quite different parts of the spectral energy distribution (see, for example, the SEDs and filter response functions for the *WISE* bands shown in Figure 19 of the Appendix). W3 is a broad filter: in the  $z \sim 0$  universe, it measures the hot/warm dust continuum including the  $7.7\ \mu\text{m}$ ,  $8.5\ \mu\text{m}$ , and  $11.3\ \mu\text{m}$  PAH (polycyclic aromatic hydrocarbon) families, but also captures nebular emission lines at  $12.81\ \mu\text{m}$  ([Ne II]) and  $13.7\ \mu\text{m}$  ([Ne III]) and the S(2) line of pure rotational hydrogen at  $12.3\ \mu\text{m}$ . PAHs are complex tracers; they are excited by starlight photons, but the resulting spectrum is highly dependent on the relative abundance and composition of the PAH population, as well as the source of excitation (see e.g. Draine et al. 2021).

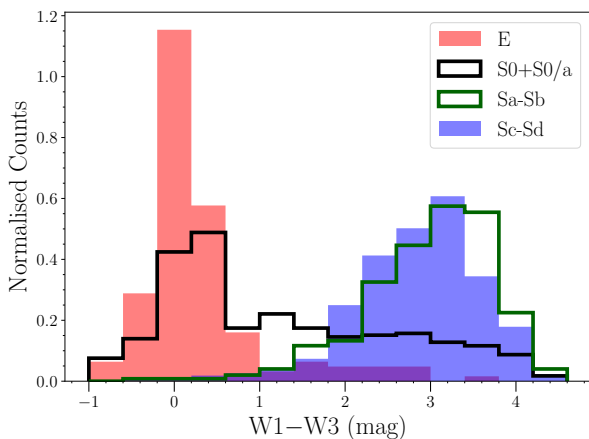


**Figure 4.** Color delineation across morphology: grouping by morphology we see that  $W1-W3$  colors separate type E, Sa-Sb and Sc-Sd reasonably well, but S0 and S0/a bulge-dominated disks tend to inhabit a broad range in color space.

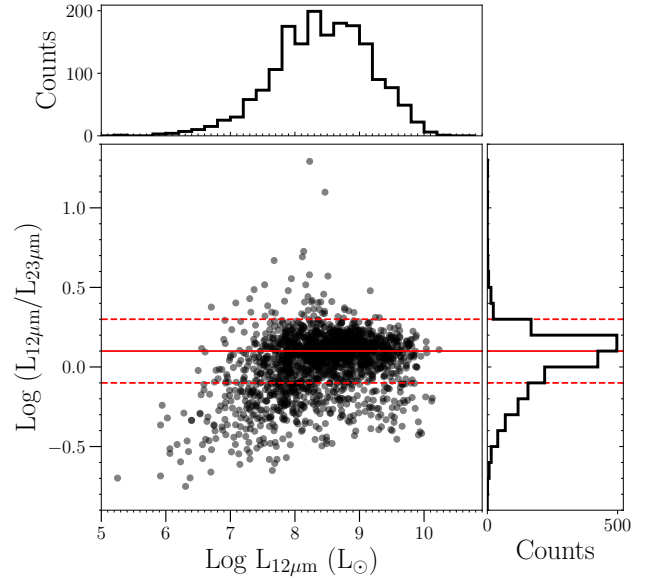


**Figure 5.** W4 “warm excess” galaxies: the ratio of  $L_{12\ \mu\text{m}}$  to  $L_{23\ \mu\text{m}}$  as a function of  $L_{12\ \mu\text{m}}$  for the S<sup>4</sup>G-*WISE* sample. The median  $\log(L_{12\ \mu\text{m}}/L_{23\ \mu\text{m}})$  value is shown as a solid line with 0.2 dex on either side as the dashed lines. The histograms of the distributions show the tail that extends to low  $\log(L_{12\ \mu\text{m}}/L_{23\ \mu\text{m}})$  values, indicating numerous sources with either a paucity in  $L_{12\ \mu\text{m}}$  emission, or a relative excess in  $L_{23\ \mu\text{m}}$ .

Although it is often assumed that the *WISE* W3 band is dominated by the  $11.3\ \mu\text{m}$  PAH at  $z \sim 0$ , as discussed in Cluver et al. (2017), its contribution is on average  $< 10\%$  and the contribution from all PAHs to W3 is on average  $< 40\%$  (based on the SINGS sample). This band is hence dominated by non-PAH continuum from stochastically heated small dust grains and the thermal emission from hot/warm dust. But, an additional consideration is the contribution from the  $10\ \mu\text{m}$  silicate absorption feature which we can expect to be prominent in compact, highly luminous sources.

In contrast, the W4 band is relatively straightforward: it samples the warm dust grain thermal continuum as well as stochastically heated very small grains. A complication for both, however, is the potential impact of dust geometry.

To investigate the geometric and environmental conditions that may affect W3 and W4 differently, we consider their luminosity ratio. We expect a range (or intrinsic scatter) that reflects the diverse conditions seen in normal galaxies, but also deviations that arise from extreme conditions (e.g., massive star formation associated with compact starbursts). In Figure 5 we plot the ratio of  $L_{12\ \mu\text{m}}$  to  $L_{23\ \mu\text{m}}$  as a function of  $L_{12\ \mu\text{m}}$ , excluding all galaxies where the log luminosity error is greater

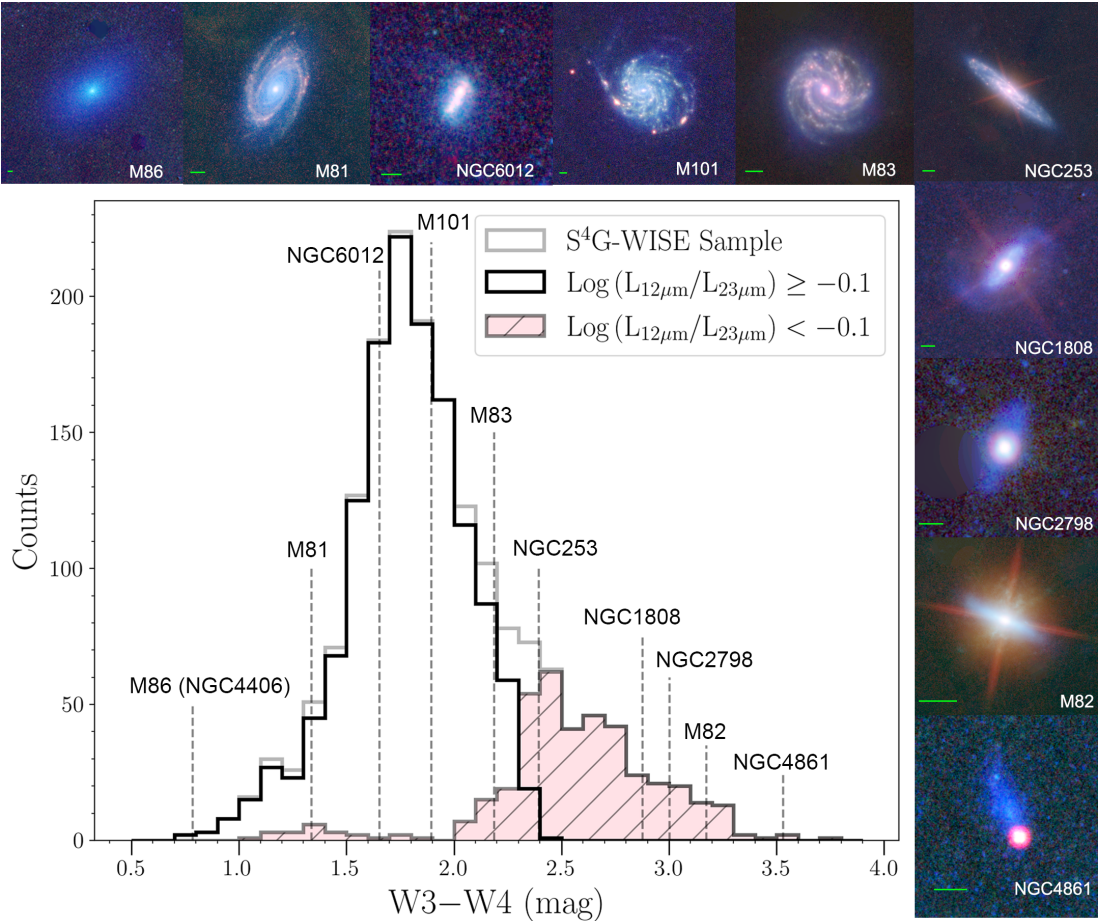


**Figure 6.** Mid-infrared “warm” galaxies: the  $W3-W4$  color distribution of  $S^4G-WISE$ , separated by  $\log(L_{12\mu m}/L_{23\mu m})$  ratio, with selected galaxies shown as four-color composite stamps combining  $W1$  (blue),  $W2$  (cyan),  $W3$  (green), and  $W4$  (red). The green bar in each image is 1 arcmin. The steep-spectrum sources, right side (shaded histogram), stand out with large  $W4$  luminosities compared to  $W3$ .

than 0.1 dex (i.e. sources with  $S/N < 5$  after removing the stellar continuum). This shows that the majority of sources cluster within  $\pm 0.2$  dex (the standard deviation) of the median value of 0.1, with outliers above and below the median distribution. However, we observe an excess in low ratio sources, forming a distinctive tail – these correspond to systems with a steeper than average mid-IR spectrum (i.e. relatively high  $L_{23\mu m}$  emission compared to  $L_{12\mu m}$ ), or alternatively, a paucity of  $W3$  emission compared to  $W4$ . These sources are found over roughly 4 orders of magnitude of  $L_{12\mu m}$  luminosity. To investigate this further, we consider the  $W3-W4$  colour distribution of the sample. This quantity is helpful to examine whether this tail is present before the stellar continuum has been subtracted from the  $W3$  and  $W4$  measurements.

In Figure 6 we examine the  $W3-W4$  colours of the entire sample, as well as the distribution when the sample is split according to the  $\log(L_{12\mu m}/L_{23\mu m})$  ratio using

a reference value of  $-0.1$  (see Figure 5). We include the locations and images of several galaxies drawn from the  $S^4G$  sample to illustrate the diversity in appearance, among them some of the most famous local galaxies. We see that  $L_{23\mu m}$  “excess” sources do, on average, lie at higher  $W3-W4$  color, similarly creating a tail in the distribution. Since we have excluded AGN “warm” sources from our analysis, a possible driver could be the star formation properties of these galaxies, analogous to the trend seen in the IRAS color of galaxies in which far-IR “warm” colors (exhibiting strong  $60\mu m$  emission relative to  $100\mu m$ ) track with massive star formation activity (see e.g. Helou 1986; Dale et al. 2001). M82, for example, with its very red  $W3-W4$  colors (i.e. steep mid-IR spectrum), is undergoing an intense nucleated starburst viewed edge-on.

The impact of including these steep spectrum sources in star formation calibrations is the topic of the next section. A more detailed analysis of the properties of

S<sup>4</sup>G-*WISE* sources based on W3–W4 are deferred to a future publication. However, we illustrate the diversity in SED shape corresponding to varying W3–W4 color in Figure A of the Appendix using NGC 1266 (lenticular hosting Seyfert nucleus), NGC 2798 (SBa undergoing tidal interaction and likely starburst), M101 (Scd and classic face-on grand-design spiral) and M81/NGC 3031 (Sab).

### 3.3. Star Formation Rates

#### 3.3.1. Revised WISE Star Formation Rate Calibrations

In Cluver et al. (2017) we derived *WISE* SFR calibrations tying  $L_{12\mu\text{m}}$  and  $L_{23\mu\text{m}}$  to  $L_{\text{TIR}}$  using the SINGS/KINGFISH sample. Although a relatively small sample of 76 galaxies, by being nearby they offered the best quality mid- and far-infrared measurements necessary to relate *WISE* fluxes to total infrared luminosity (using the measurements from Dale et al. 2017). In this section, we repeat the analysis from Cluver et al. (2017) but make a distinction between sources based on their  $L_{12\mu\text{m}}/L_{23\mu\text{m}}$  ratio. Revisiting this analysis benefits from improved resolved source photometry of all sources (54 of which are part of S<sup>4</sup>G-*WISE*) as the WXSC pipeline has matured, as well as the improved implementation of distances by incorporating more robust redshift-independent measures. The *WISE* color-color diagram and W3–W4 color distribution for the SINGS/KINGFISH sample are included in Section A of the Appendix.

As in Cluver et al. (2017), we derive  $L_{\text{TIR}}$  using Equation 5 of Dale et al. (2014) which combines  $8\mu\text{m}$ ,  $24\mu\text{m}$ ,  $70\mu\text{m}$ , and  $160\mu\text{m}$  using the SINGS/KINGFISH photometry presented in Dale et al. (2017). We convert this to a SFR using the relation (Equation 3) of Calzetti (2013), which uses the Starburst99 models (Leitherer et al. 1999) assuming Solar metallicity, constant star formation over  $t = 100$  Myr, and a Kroupa (2001) IMF:

$$\text{SFR}(M_{\odot} \text{ yr}^{-1}) = 2.8 \times 10^{-44} L_{\text{TIR}} \text{ (erg.s}^{-1}\text{)}. \quad (2)$$

Figure 7a plots the relationship between  $\log \text{SFR}_{\text{TIR}}$  and  $\log L_{12\mu\text{m}}$  color-coded by  $L_{12\mu\text{m}}/L_{23\mu\text{m}}$  ratio. Somewhat surprisingly, the relationship between  $L_{12\mu\text{m}}$  and  $\text{SFR}_{\text{TIR}}$  appears largely agnostic to this quantity. The one significant outlier is NGC 1266, likely harboring an AGN (e.g. Alatalo et al. 2011). The best-fit line and SFR relation is given by:

$$\text{Log SFR}(M_{\odot} \text{ yr}^{-1}) = 0.89(\pm 0.02) \text{Log } L_{12\mu\text{m}}(L_{\odot}) - 7.93(\pm 0.20) \quad (3)$$

with a  $1\sigma$  scatter of 0.10 dex.

By contrast, Figure 7b reveals that what was thought to be increased scatter in Cluver et al. (2017) can be attributed to two “flavours” of sources, with  $\log(L_{12\mu\text{m}}/L_{23\mu\text{m}}) < -0.1$  galaxies being systematically lower in the  $\log \text{SFR}_{\text{TIR}}$  versus  $\log L_{23\mu\text{m}}$  diagram. In reality, we imagine a continuum of values, but as a first step we fit each population separately resulting in updated  $\text{SFR}_{23\mu\text{m}}$  relations as follows:

$$\text{Log SFR}(M_{\odot} \text{ yr}^{-1}) = 0.91(\pm 0.03) \text{Log } L_{23\mu\text{m}}(L_{\odot}) - 8.02(\pm 0.23) \quad (4)$$

with a  $1\sigma$  scatter of 0.12 dex for “nominal” mid-infrared sources, i.e.  $\log(L_{12\mu\text{m}}/L_{23\mu\text{m}}) \geq -0.1$ , and,

$$\text{Log SFR}(M_{\odot} \text{ yr}^{-1}) = 0.89(\pm 0.02) \text{Log } L_{23\mu\text{m}}(L_{\odot}) - 8.18(\pm 0.19) \quad (5)$$

with a  $1\sigma$  scatter of 0.14 dex for “warm” mid-infrared sources, i.e.  $\log(L_{12\mu\text{m}}/L_{23\mu\text{m}}) < -0.1$ .

The intermediate relationship between  $L_{\text{TIR}}$  and  $L_{12\mu\text{m}}$  and  $L_{23\mu\text{m}}$ , respectively, is shown in Figure 18 and provided as Equations A1 for  $L_{12\mu\text{m}}$  and A2 and A3 for  $L_{23\mu\text{m}}$  in the Appendix.

Next, in Figure 8, we compare the  $L_{12\mu\text{m}}$  and  $L_{23\mu\text{m}}$  derived SFRs and find much better agreement than in Cluver et al. (2017). We note the outlier in Figure 8b with a  $\log \text{SFR}_{12\mu\text{m}} - \log \text{SFR}_{23\mu\text{m}}$  value of  $-0.38$ , NGC 1266. Although this galaxy has a warm W1–W2 color, it does not exceed our threshold (see Figure 17a) but is known to harbor an obscured AGN (Alatalo et al. 2011). The steep spectrum of NGC 1266 means that its  $23\mu\text{m}$  derived SFR is  $1.55 M_{\odot} \text{ yr}^{-1}$ , compared to the  $12\mu\text{m}$  derived value is  $0.65 M_{\odot} \text{ yr}^{-1}$ . We include an SED of this source in Figure A of the Appendix, clearly showing it to be one of the steepest sources in the sample (see also Figure 6 in Dale et al. 2007).

The improved calibration of SFR using  $L_{12\mu\text{m}}$  and  $L_{23\mu\text{m}}$  allows us to combine these using inverse-variance weighting (photometric + fitting uncertainties), since they are calibrated to the same system and do not appear to vary systematically; we designate this combined SFR as  $\text{SFR}_{\text{MIR}}$ . Of course, this all hinges on how well  $L_{\text{TIR}}$  captures star formation and we remind the reader that the use of *WISE* as a SFR indicator should be an informed choice. We investigate this further in the following section.

#### 3.3.2. Calibration to Hybrid UV+IR SFRs

Although the mid-infrared can be considered a reasonable predictor of SFR for most star-forming galaxies, it

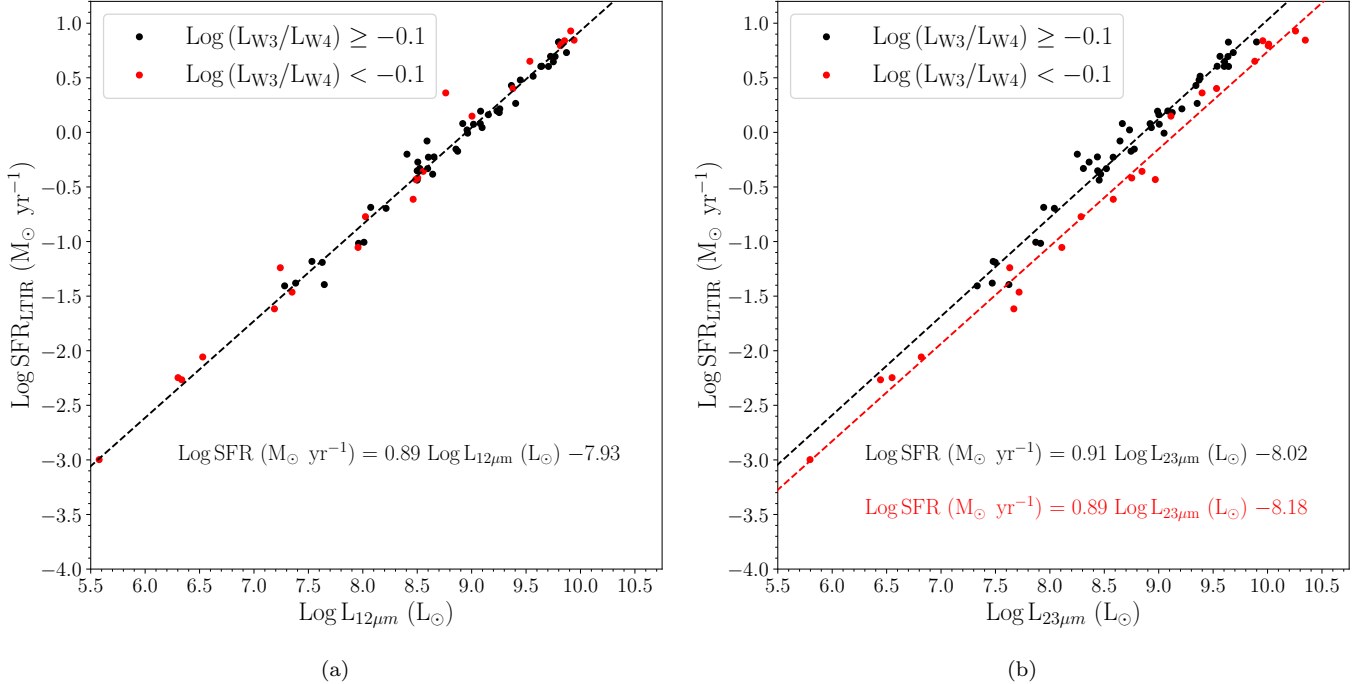


**Figure 7.** How the mid-IR tracks with the total-infrared SFR: (a) The relationship between  $12\mu\text{m}$  luminosity and SFR (calibrated to total infrared luminosity) using the SINGS/KINGFISH sample, with sources color-coded by  $\log(L_{12\mu\text{m}}/L_{23\mu\text{m}})$  ratio. The best fit adequately describes both red (warm) and black (normal) sources. (b) Considering the relationship between  $\text{SFR}_{\text{TIR}}$  and  $L_{23\mu\text{m}}$  we see that black sources ( $\log(L_{12\mu\text{m}}/L_{23\mu\text{m}}) \geq -0.1$ ) and red sources ( $\log(L_{12\mu\text{m}}/L_{23\mu\text{m}}) < -0.1$ ) can be described by two separate relations thus reducing the overall scatter. This suggests that steep mid-IR spectrum sources correspond to a lower  $\text{SFR}_{\text{TIR}}$  than would be inferred by the  $23\mu\text{m}$  emission without taking this into account i.e. they follow a different scaling relation.

will underestimate the SFR of low stellar mass galaxies with relatively low metallicity and dust content. At the other end of the mass spectrum, it will overestimate the current SFR where dust from past star formation is being preferentially heated by old stars (in this case an overly delayed measure of star formation). To investigate this further we exploit the UV data available for S<sup>4</sup>G.

Bouquin et al. (2018) present the GALEX-S<sup>4</sup>G sample which furnishes GALEX FUV and NUV photometry for 1931 galaxies in S<sup>4</sup>G. We make use of these measurements to explore hybrid calibrations that leverage tracers of both dust unobscured and obscured star formation.

The FUV and NUV photometry is taken from Bouquin et al. (2018) and reddening-corrected using the recommended values from Wyder et al. (2007) derived using a Cardelli et al. (1989) extinction law. Galactic reddening is corrected using the relations from Peek & Schiminovich (2013) following Salim et al. (2016).

In Figure 9a we use the hybrid FUV+W4 SFR indicator from Belfiore et al. (2023) to examine the difference in SFR rate compared to  $\text{SFR}_{12\mu\text{m}}$ , derived in the pre-

vious section, as a function of  $M_{\text{stellar}}$ . There is a pronounced deviation for masses  $\text{Log } M_{\text{stellar}} < 9.9$ , where  $\text{SFR}_{12\mu\text{m}}$  is progressively underestimating the SFR. The question arises as to whether this paucity in dust emission can be quantified. In Figure 9b we plot the SFR difference as a function of  $L_{\text{W3}}$  luminosity density, or  $\Sigma_{12\mu\text{m}}$  ( $L_{\odot}/\text{kpc}^2$ ). This corresponds to  $L_{12\mu\text{m}}$ , i.e. W3 emission with the stellar contribution removed, normalised by the area of the galaxy (in  $\text{kpc}^2$ ) as measured in W1 (which traces the entire stellar disk). We see that for sources with  $\text{Log } M_{\text{stellar}} \geq 9.9$  the points cluster around 0, but for  $\text{Log } M_{\text{stellar}} < 9.9$  the offset increases, also reflected by the decreasing W1–W3 color indicating more stellar-dominated emission. This deviation can be described by the following function:

$$\text{Log SFR}_{\text{deficit}} = a + b \text{Log } \Sigma_{12\mu\text{m}} + c (\text{Log } \Sigma_{12\mu\text{m}})^2, \quad (6)$$

where  $a = 7.56$ ,  $b = -1.94$ , and  $c = 0.119$ .

If we apply this as:

$$\text{Log SFR}_{12\mu\text{m},\text{corr}} = \text{Log SFR}_{12\mu\text{m}} + \text{Log SFR}_{\text{deficit}} \quad (7)$$

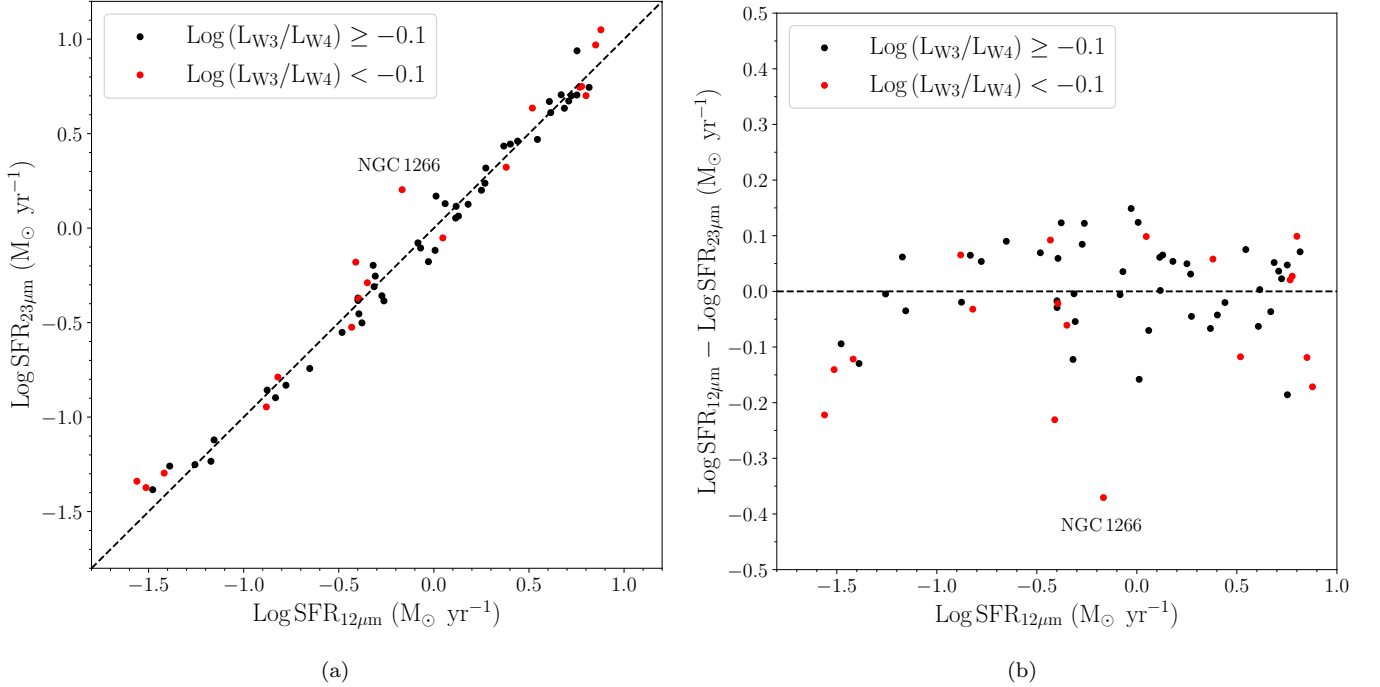


**Figure 8.** Comparing the  $L_{12\mu\text{m}}$  and  $L_{23\mu\text{m}}$  SFRs: (a) Using the SFR calibrations presented in Figure 7, i.e. making the distinction based on  $L_{12\mu\text{m}}/L_{23\mu\text{m}}$  for  $\text{SFR}_{23\mu\text{m}}$ , we find good agreement between  $\text{SFR}_{12\mu\text{m}}$  and  $\text{SFR}_{23\mu\text{m}}$ . The dashed line indicates one-to-one correspondance. (b) The comparison between  $\text{SFR}_{12\mu\text{m}}$  and  $\text{SFR}_{23\mu\text{m}}$  indicates that for  $\log(L_{12\mu\text{m}}/L_{23\mu\text{m}}) \geq -0.1$  sources the agreement is within  $\pm 0.15$  dex. Galaxy NGC 1266 is the low-value outlier.

for sources with  $\text{Log } M_{\text{stellar}} < 9.9 M_{\odot}$  and where  $\text{Log } \Sigma_{12\mu\text{m}} < 6.5 L_{\odot}/\text{kpc}^2$  (see Figure 9b), the result is shown in Figure 9c.

Similarly we can define:

$$\text{Log SFR}_{23\mu\text{m},\text{corr}} = \text{Log SFR}_{23\mu\text{m}} + \text{Log SFR}_{\text{deficit}} \quad (8)$$

In the absence of UV information, one can therefore estimate the degree to which the *WISE*-derived SFRs are underestimating the total SFR. We caution that for any one source, there would be a high degree of uncertainty, but for studying the behaviour of large populations it provides a more accurate reflection of the SFR for the low mass population in the absence of UV photometry. We also note that  $\text{Log } \Sigma_{12\mu\text{m}}$  is by its nature a global measurement, essentially scaling with the dust mass (see below), and is designed as a broad indicator of the dust deficit, and hence SFR deficit in the low dust regime.

We note that there are sources in Figure 9c where  $\text{SFR}_{12\mu\text{m},\text{corr}}$  appears to be an overestimate compared to  $\text{SFR}_{\text{FUV+W4}}$ ; these are analysed further in Section C of the Appendix, which suggests that the UV emission is low compared to both  $12\mu\text{m}$  and  $23\mu\text{m}$  and (importantly) there is no correlation with stellar mass.

To further investigate the  $\Sigma_{12\mu\text{m}}$  quantity, we make use of the DustPedia project (Davies et al. 2017), which has 725 galaxies in common with S<sup>4</sup>G, and has SED-derived properties (Nersesian et al. 2019) modelled using CIGALE (Boquien et al. 2019); we use the outputs derived using the Draine et al. (2014) dust model.

Figure 9d makes a comparison of  $\text{Log } \Sigma_{12\mu\text{m}}$  and SED-derived dust mass, which we would expect to be correlated. Indeed we see that the quantities do track each other despite the relatively simple nature of the  $\text{Log } \Sigma_{12\mu\text{m}}$  metric. Of course, the latter is only feasible in the low-redshift Universe where the isophotal size of the galaxy has been carefully measured.

In Figure 10 we show the comparison of  $\text{SFR}_{12\mu\text{m},\text{corr}}$  and  $\text{SFR}_{23\mu\text{m},\text{corr}}$  for the S<sup>4</sup>G-*WISE* sample, excluding sources with low S/N measurements ( $S/N < 5$ ). Further comparisons of  $\text{SFR}_{12\mu\text{m},\text{corr}}$  with several hybrid UV+IR from the literature can be found in Figure C of the Appendix.

We next investigate  $\Sigma_{12\mu\text{m}}$ , and similarly,  $\Sigma_{23\mu\text{m}}$  as an ISM activity metric; in Figure 11a and b we see that these quantities broadly track the ratio of dust to FUV luminosity as traced by  $L_{12\mu\text{m}}$  and  $L_{23\mu\text{m}}$ , for galaxies with  $\text{Log } M_{\text{stellar}} < 9.9$  (where we have also applied a T-type  $> 0.5$  requirement to remove low mass spheroidals).

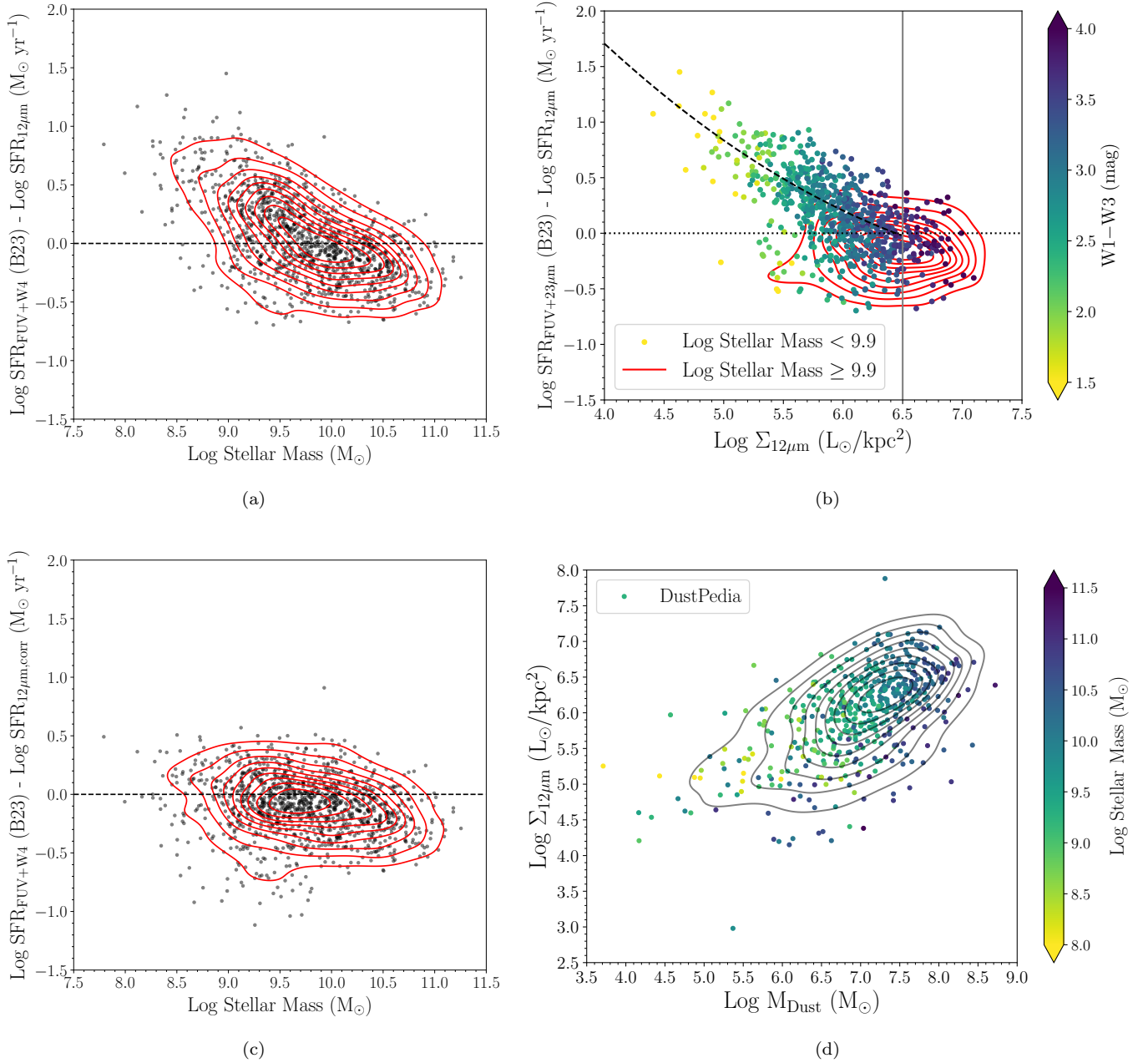


**Figure 9.** Assessing the relative difference between the UV and infrared SF tracers: (a) The difference between  $\text{SFR}_{\text{FUV+W4}}$  using the relation from Belfiore et al. (2023) and  $\text{SFR}_{12\mu\text{m}}$  as function of stellar mass. (b) The difference between  $\text{SFR}_{\text{FUV+W4}}$  using the relation from Belfiore et al. (2023) and  $\text{SFR}_{12\mu\text{m}}$  as function of  $12\mu\text{m}$  dust density ( $\Sigma_{12\mu\text{m}}$  showing that sources with  $\log M_{\text{stellar}} < 9.9$  show progressively lower  $\text{SFR}_{12\mu\text{m}}$  compared to  $\text{SFR}_{\text{FUV+W4}}$  as a function of  $\Sigma_{12\mu\text{m}}$ . (c) After applying a correction derived from Figure 9b, the correspondence between  $\text{SFR}_{12\mu\text{m}}$  compared to  $\text{SFR}_{\text{FUV+W4}}$  as a function of stellar mass is vastly improved. (d) Using sources in common with the DustPedia project we find a correspondence between  $\Sigma_{12\mu\text{m}}$  and dust mass as derived from SED-fitting using CIGALE.

The  $L_{12\mu\text{m}}/L_{\text{FUV}}$  and  $L_{23\mu\text{m}}/L_{\text{FUV}}$  ratios for the full *S4G-WISE* UV sample (split by morphology) are included in Section D of the Appendix; this shows that the dust to UV ratios are well-correlated to dust con-

tent for late-type galaxies, but show progressively more scatter with earlier types.

The relationship between  $L_{\text{TIR}}$  and  $L_{12\mu\text{m}}$  (Equation A1 of the Appendix) can be used to approximate the infrared excess ( $\text{IRX} \equiv L_{\text{TIR}}/L_{\text{FUV}}$ ); this is shown in Fig-

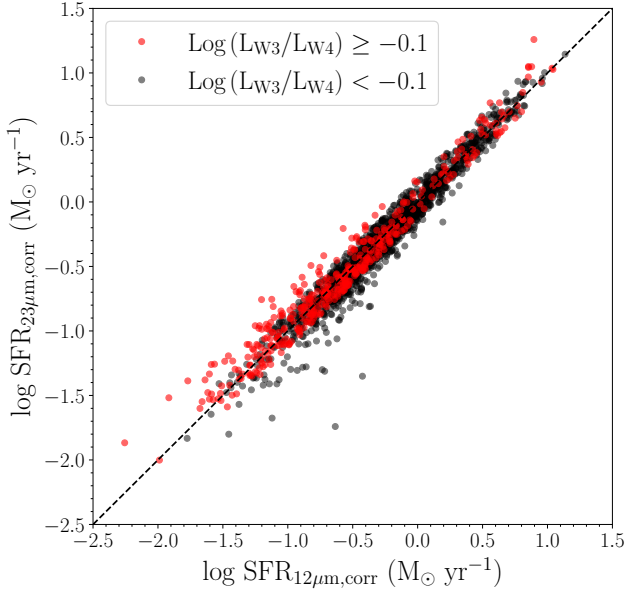


**Figure 10.** Similar to Figure 8a, but now with the entire S<sup>4</sup>G-*WISE* sample, and using the  $\text{SFR}_{\text{deficit}}$  correction, we observe the relatively close correspondence between  $\text{SFR}_{12\mu\text{m},\text{corr}}$  and  $\text{SFR}_{23\mu\text{m},\text{corr}}$ .

ure 12 as a function of  $M_{\text{stellar}}$  separated by morphological type, where we include the relations from Hunt et al. (2019), derived using a  $z \sim 0$  sample, and from Bouwens et al. (2016) derived for  $z = 2 - 10$ , for comparison. The agreement appears closest with the Bouwens et al. (2016) relation, and perhaps unsurprisingly, for the Sc morphological types, but we note that our sample lacks power at the high mass end ( $\log M_{\text{stellar}} > 10.5$ ). We see that some bulge-dominated (E/S0/S0-a and Sa) galaxies are represented, albeit with larger scatter in the distribution compared to disk-dominated morphologies (Sb to Sd). Noting these are predominately not high mass systems ( $\log M_{\text{stellar}} > 11$ ), the dust and UV properties of these “early types” are not consistent with being passive systems. This is discussed further in Section D of the Appendix, but a more complete analysis of these systems is deferred to a future publication.

### 3.3.3. Comparison to DustPedia CIGALE-derived SFRs

As mentioned in the previous section, S<sup>4</sup>G-*WISE* has 725 galaxies in common with the nearby galaxy DustPedia project (Davies et al. 2017) where SED-fitting of multiband photometry (Nersesian et al. 2019) using CIGALE (Boquien et al. 2019) can provide an additional test of the *WISE*-derived SFRs.

In order to compare SFRs we select sources with well-measured  $L_{12\mu\text{m}}$  and  $L_{23\mu\text{m}}$  ( $S/N > 5$ ) and with DustPedia SFRs with errors  $< 40\%$ . In Figure 13a and b

we compare the deficit-corrected *WISE*-derived SFRs to the CIGALE-derived values, color-coded by  $\log M_{\text{stellar}}$ . Both  $\text{SFR}_{12\mu\text{m},\text{corr}}$  and  $\text{SFR}_{23\mu\text{m},\text{corr}}$  show good agreement with CIGALE-derived star formation rates. It is encouraging that we do not see clear deviation at low levels of SFR, a regime where SFR indicators can produce significantly different values (see Li et al. 2023). However, our relatively small sample size is a clear limitation.

In Figure 13c and d we consider the comparison of DustPedia-derived SFRs to  $\text{SFR}_{\text{MIR}}$ , which is the inverse-variance weighted combination of  $\text{SFR}_{12\mu\text{m}}$  and  $\text{SFR}_{23\mu\text{m}}$ , and  $\text{SFR}_{\text{MIRcorr}}$  which is the inverse-variance weighted combination of  $\text{SFR}_{12\mu\text{m},\text{corr}}$  and  $\text{SFR}_{23\mu\text{m},\text{corr}}$ . As a function of  $M_{\text{stellar}}$ , we see that  $\text{SFR}_{\text{MIR}}$  clearly underestimates the SFR at low mass (Figure 13c); this effect is largely ameliorated in Figure 13d after applying the  $\text{SFR}_{\text{deficit}}$  correction (as presented in the previous section). In this figure, galaxies have been color-coded by W1–W3 color which indicates good agreement between the two SFR methods, irrespective of star formation activity (where W1–W3 acts a proxy for specific star formation). In particular, we do not see a clear overestimation of SFR determined using the mid-IR at high  $M_{\text{stellar}}$ , which could be ascribed to dust heated by old stars, as opposed to tracing recent star formation. However, we note that the S<sup>4</sup>G sample does not contain many high  $M_{\text{stellar}}$  galaxies and the limited sample overlap of DustPedia and S<sup>4</sup>G in this regime does not provide a fully reliable test. The accuracy of *WISE*-derived SFRs in the high  $M_{\text{stellar}}$  regime will be investigated in a future study using a larger sample drawn from the WXSC (notably including galaxies from the 2MRS; Huchra et al. 2012).

### 3.4. Stellar Mass and Star Formation in the Nearby Universe

In this section we examine the relationship between star formation and stellar mass in the S<sup>4</sup>G sample. We derive *WISE* stellar masses using the prescription of Jarrett et al. (2023), but since the *WISE*-derived SFRs assume a Kroupa (2001) IMF, we apply a conversion to a Chabrier (2003) IMF using the offsets from Zahid et al. (2012) to be fully consistent (corresponding to a near negligible shift of 0.03 dex).

In Figure 14 we plot the S<sup>4</sup>G sample in the  $\log \text{SFR}_{\text{MIRcorr}} - \log M_{\text{stellar}}$  plane. We make the distinction between low S/N sources (where either  $L_{12\mu\text{m}}$  or  $L_{23\mu\text{m}}$  have a  $S/N < 5$ ) and well-determined SFRs in the sample, and also indicate sources where only an upper limit for the SFR is achievable. The latter does not necessarily mean the original detection W3 detection is

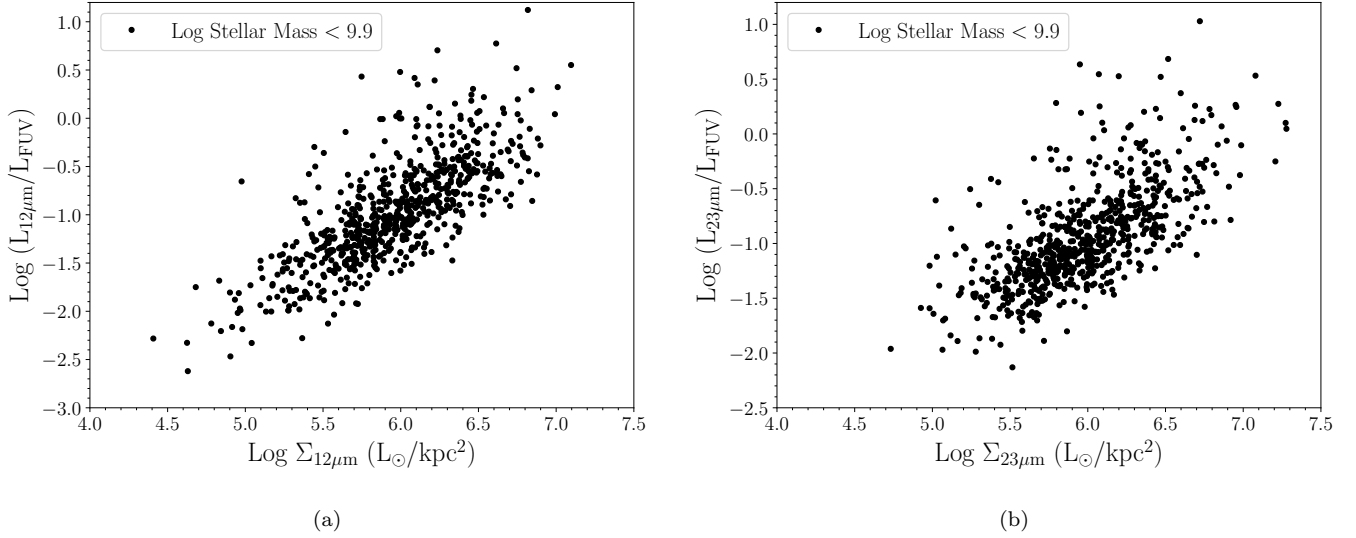


**Figure 11.** The effect of dust density on the infrared-to-FUV correlation: for sources with  $\log M_{\text{stellar}} < 9.9$ , we show in (a) the broad correspondence between  $L_{12\mu\text{m}}/L_{\text{FUV}}$  and  $\Sigma_{12\mu\text{m}}$ , and in (b) the relationship between  $L_{23\mu\text{m}}/L_{\text{FUV}}$  and  $\Sigma_{23\mu\text{m}}$ . The latter appears to show more scatter, likely driven by the poorer sensitivity of the W4 band.

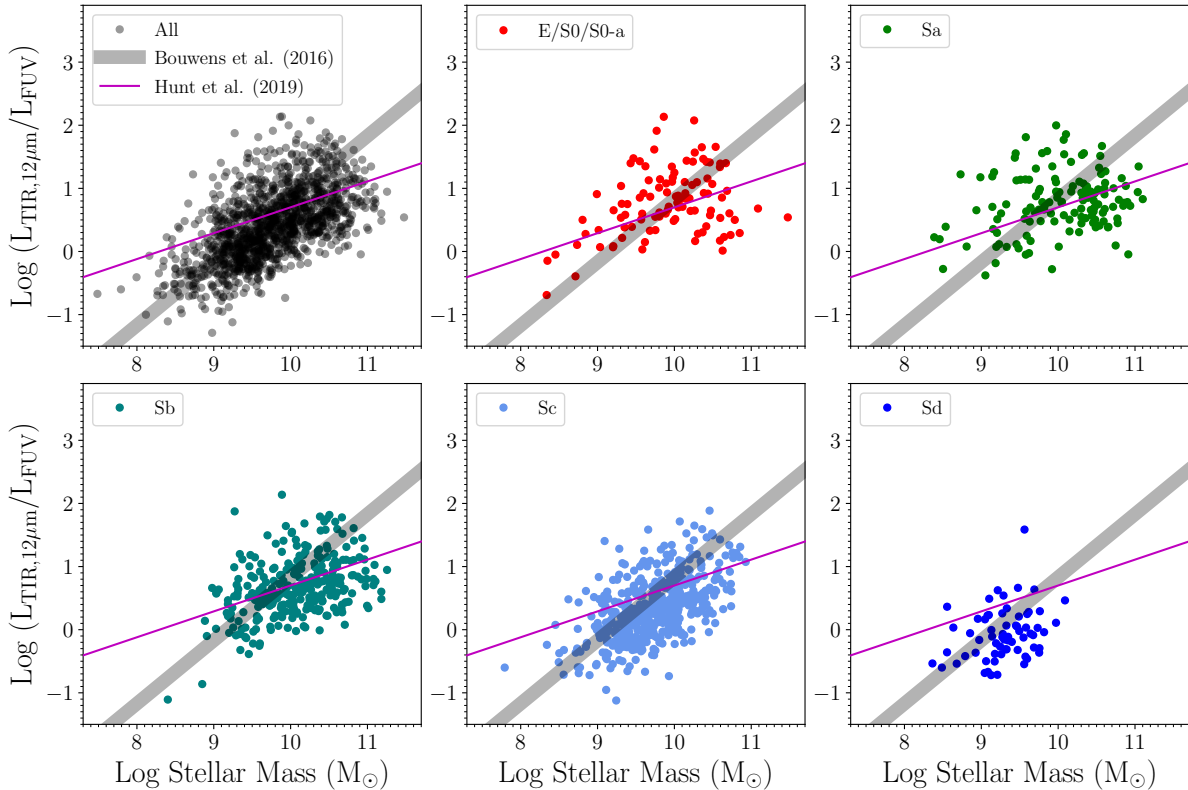


**Figure 12.** Morphology and the infrared-to-UV correlation: using the relationship between  $L_{12\mu\text{m}}$  and  $L_{\text{TIR}}$  (see Section A of the Appendix), we calculate the proxy  $L_{\text{TIR},12\mu\text{m}}/L_{\text{FUV}}$  ratio for our sample (top left panel) and then separated by morphological type. The relations from Bouwens et al. (2016) and Hunt et al. (2019) are shown for comparison. See also the similar diagrams in the Appendix, Figures 22 and 23, showing this ratio as a function of the dust density.

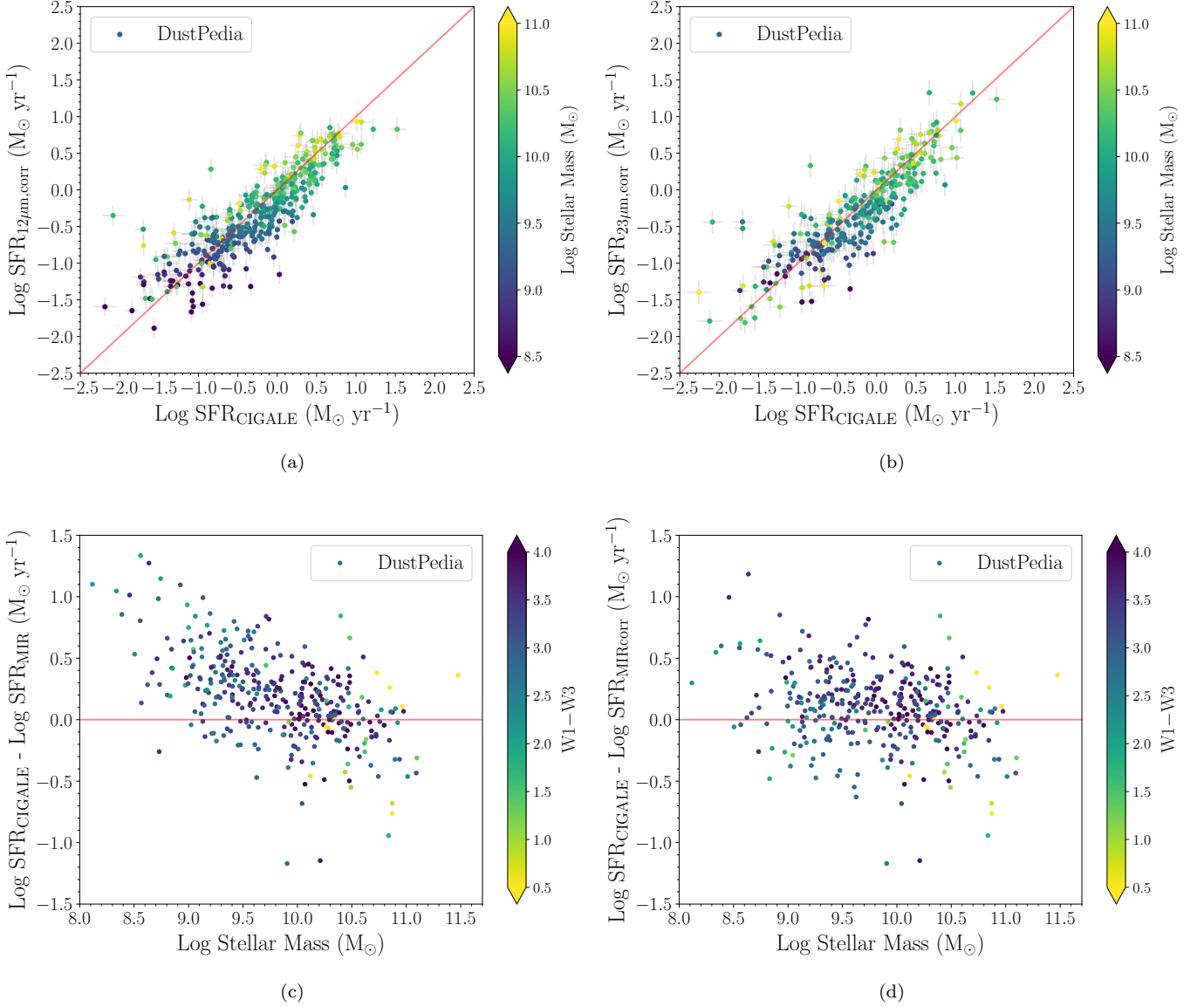


**Figure 13.** Comparison between CIGALE-derived SFRs from DustPedia with (a)  $\text{SFR}_{12\mu\text{m,corr}}$  and (b)  $\text{SFR}_{23\mu\text{m,corr}}$ . In (c) we compare  $\text{SFR}_{\text{CIGALE}}$  to the inverse-variance weighted combination of  $\text{SFR}_{12\mu\text{m}}$  and  $\text{SFR}_{23\mu\text{m}}$  ( $\text{SFR}_{\text{MIR}}$ ), i.e. with no correction applied at low mass, as a function of  $\text{log } M_{\text{stellar}}$ . We see that the clear deficit observed is largely ameliorated in (d) which instead compares  $\text{SFR}_{\text{CIGALE}}$  to the inverse-variance weighted combination of  $\text{SFR}_{12\mu\text{m,corr}}$  and  $\text{SFR}_{23\mu\text{m,corr}}$  ( $\text{SFR}_{\text{MIRcorr}}$ ) as a function of  $\text{log } M_{\text{stellar}}$ .

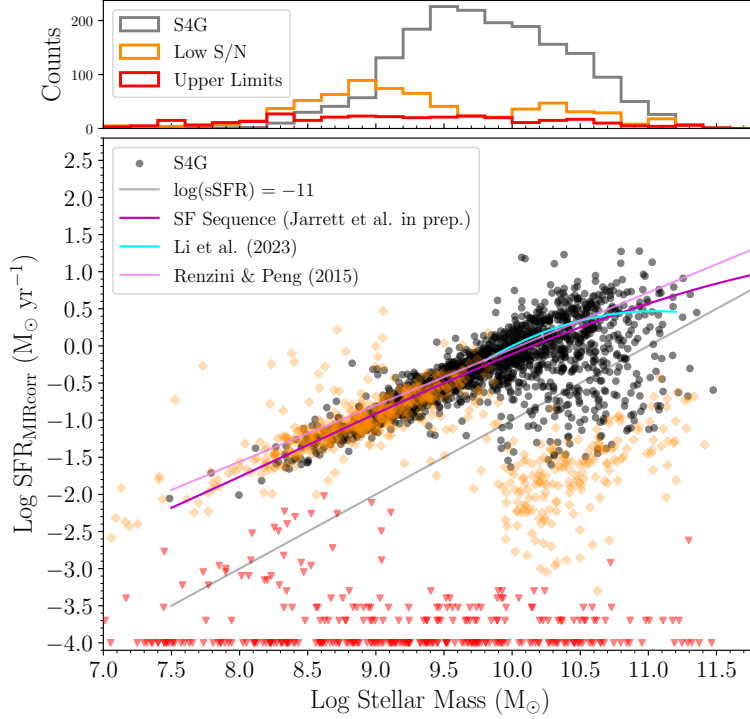


**Figure 14.** The Star-forming “Main Sequence”, showing star formation relative to star formation history, for the  $S^4G$ -*WISE* sample. The fit derived using a large sample from the 2MRS (Jarrett et al., in prep.) is shown in magenta, the relation of Renzini & Peng (2015) in pink and Li et al. (2023) in cyan. Low S/N sources (where either  $L_{12\mu m}$  or  $L_{23\mu m}$  have a  $S/N < 5$ ) are shown in orange, and upper limits as red triangles.

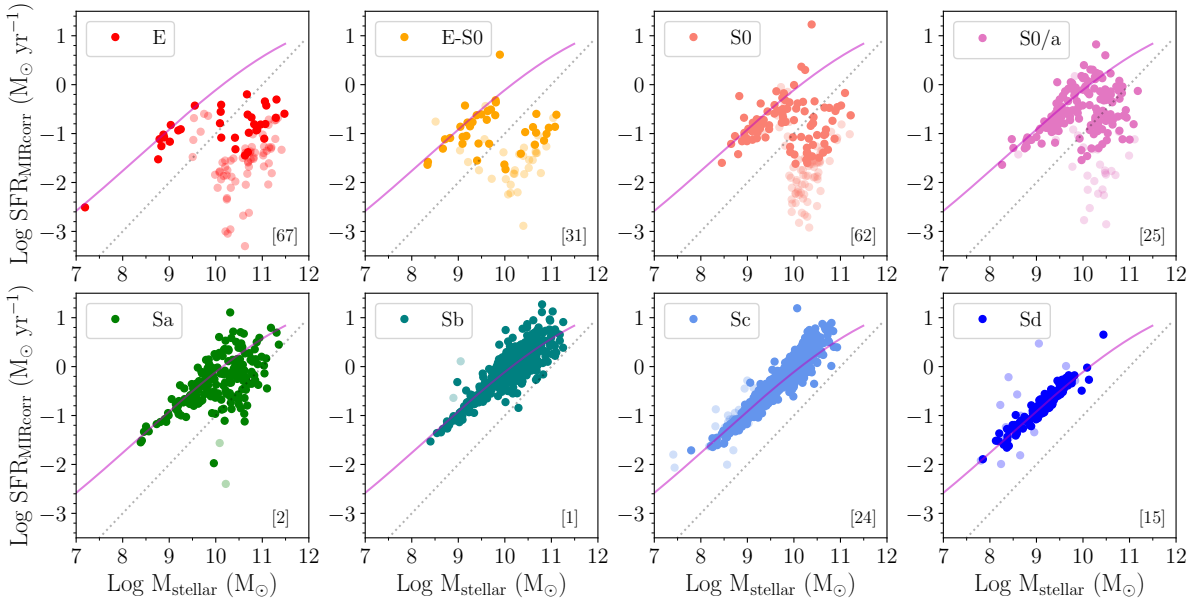


**Figure 15.** Examining the location of different morphological types in the SFR- $M_{\text{stellar}}$  plane, the SFMS line from the previous figure (Jarrett et al., in prep.) is shown as the magenta line, and  $\log \text{SFR}/M_{\text{stellar}} = -11$  as the dotted grey line. Low S/N sources (where either  $L_{12\mu m}$  or  $L_{23\mu m}$  has a  $S/N < 5$ ) are shown as transparent points, indicating that even given the proximity of the  $S^4G$  sample, low levels of star formation are largely associated with low confidence measurements. The number in the bottom right of each panel reflects the number of galaxies not shown since they are star formation non-detections.

low S/N, but could instead arise where the stellar con-

tinuum was the dominant source of flux in the band.

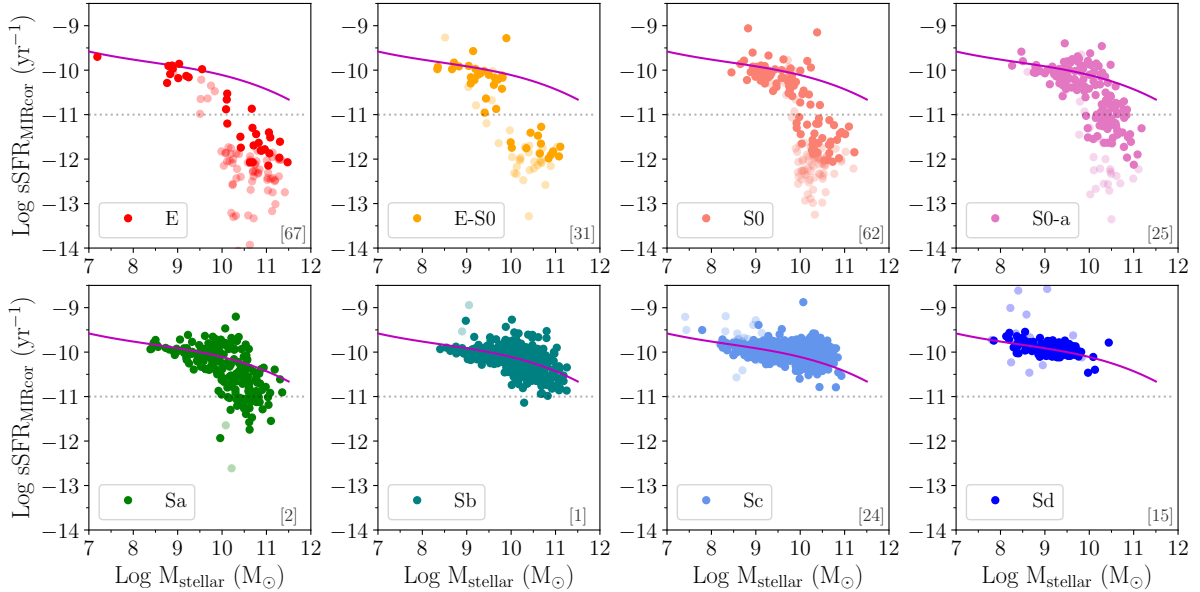


**Figure 16.** Same as the previous figure, but now showing specific SFR, i.e.  $\log \text{SFR}/M_{\text{stellar}}$  on the y-axis. This more clearly shows the correlation between morphology and galaxies moving off the so-called SFMS.

Low S/N sources appear at both low and high mass reflecting two different low star formation regimes, where the former may be the result of low dust content in low metallicity, but actively star-forming low mass galaxies. We also show the so-called Star forming Main Sequence (SFMS) fit from Jarrett et al. (in prep.) which is derived by combining the S<sup>4</sup>G sample with  $\sim 14\,000$  sources from the 2MASS Redshift Survey (Huchra et al. 2012); this fit shows excellent agreement with the star-forming galaxies in S<sup>4</sup>G.

The division between efficiently star-forming galaxies and those that have moved off the SFMS is often delineated using specific star formation rate (sSFR;  $\log \text{SFR}/M_{\text{stellar}}$ ), for example,  $\log \text{SFR}/M_{\text{stellar}} = -11$  (e.g. Wetzel et al. 2012; Houston et al. 2023); this is indicated on Figure 14 as the grey line.

Examining the location of sources in Figure 14, we see that even given the proximity of the S<sup>4</sup>G sample, low levels of measured star formation for  $\text{Log } M_{\text{stellar}} > 10$  are predominantly associated with low S/N sources. We therefore caution users from interpreting very low WISE-derived SFRs ( $\log \text{SFR} < -2$ ) as these may be spurious measurements or reflect low levels of dust emission that may not be associated with recent star formation. In any event, these galaxies have star formation activity well below the line used to delineate galaxies that have moved off the SFMS. The number of galaxies without detectable star formation (and which are therefore not shown) are indicated by the number in the bottom right corner of each plot.

We next sub-divide the S<sup>4</sup>G-WISE sample by morphological type, showing the  $\text{Log SFR}-\text{Log } M_{\text{stellar}}$  plane in Figure 15 and  $\text{Log sSFR}-\text{Log } M_{\text{stellar}}$  plane in Figure 16. This shows that disk-dominated galaxies (Sc and Sd) exhibit a tight locus around the SFMS. The addition of a more prominent bulge (Sa and Sb) appears to effectively broaden the distribution of the star-forming population, with galaxies increasingly leaving the SFMS as they become bulge-dominated (from S0/a to E), reflecting their decreased likelihood of exhibiting active star formation. The nature of the dust emission in particularly the E and S0 populations, and for example what an appropriate W1–W3 color cut would be to distinguish passively heated dust from active star formation, will be the subject of a future publication.

As noted in section 3.1, the S0 and S0/a population occupies a broad range of W1–W3 color; we see that this behaviour is consistent with what is observed in the  $\text{Log SFR}-\text{Log } M_{\text{stellar}}$  plane, i.e. showing widely distributed star-forming properties relative to stellar mass content.

Figure 16, employing sSFR in place of SFR, more clearly shows the transition from the star-forming sequence to being “quenched”. In Table 1 we summarise the total number of galaxies in each morphological type, the percentage that lie within the star-forming sequence (i.e. above  $\log \text{SFR}/M_{\text{stellar}} = -11$ ), those below, and galaxies where no star formation was detected. Given the proximity of the sample, galaxies classified as Sc and Sd with non-detectable star formation is likely due

to relatively low dust content, and not necessarily the absence of star formation (as would be more likely true of the early-type systems).

#### 4. DISCUSSION

The S<sup>4</sup>G-*WISE* sample underscores the dichotomy of complexity in the dust properties of galaxies in the nearby Universe; we see that morphology, stellar mass and dust density can produce clear correlations, or conversely, large variations. Central to this work, we have re-evaluated the relationship between  $L_{\text{TIR}}$  and  $L_{12\mu\text{m}}$  and  $L_{23\mu\text{m}}$ , respectively, and derived updated SFR scaling relations with the option of using dust density as a metric for estimating the deficit due to the contribution of unobscured star formation in low mass ( $\log M_{\text{stellar}} < 9.9 M_{\odot}$ ), low dust galaxies.

Of course, the use of *WISE* as a SFR tracer relies on how well the reprocessing of recent star formation is captured by dust emission, with the contribution of old stars to the heating of dust as an important source of uncertainty (e.g. Boquien et al. 2016). This is particularly important when PAHs are concerned (e.g. Zhang & Ho 2023; Calzetti et al. 2024) and although, as discussed earlier, the *WISE* W3 band is not dominated by PAH emission, it is certainly a significant contributor.

The S<sup>4</sup>G-*WISE* sample does not have sufficient numbers of high mass galaxies ( $\log M_{\text{stellar}} > 10.5 M_{\odot}$ ) to explore this fully, but examining Figures 22 and 23 of the Appendix, we see that earlier morphological types (irrespective of total stellar mass) show distributions with, on average, elevated  $\log(L_{12\mu\text{m}}/L_{\text{FUV}})$  and  $\log(L_{23\mu\text{m}}/L_{\text{FUV}})$  ratios as a function of dust density ( $\Sigma_{12\mu\text{m}}$  and  $\Sigma_{23\mu\text{m}}$ , respectively). This may be indicative of dust heated by evolved stellar populations (in this case, correlated with increasing bulge prominence) which would lead to an overestimation of mid-infrared derived star formation rates. Quantification and potential mitigation of such an effect is beyond the scope of this work; this would require detailed radiative transfer modelling (e.g. Baes et al. 2011) to disentangle the effects of dust attenuation, dust geometry and the heating from different generations of stellar populations.

What we have shown is that the low scatter in the correlation of  $L_{\text{TIR}}$  and  $L_{12\mu\text{m}}$  can be replicated in  $L_{23\mu\text{m}}$  and  $L_{\text{TIR}}$  by taking into account the steepness of the warm dust continuum (or, alternatively, the paucity of  $12\mu\text{m}$  emission) as traced by W3–W4, or alternately,  $L_{12\mu\text{m}}/L_{23\mu\text{m}}$ . Given the better sensitivity of W3, having an estimate of  $L_{\text{TIR}}$  in support of large galaxy surveys is arguably more powerful than merely being a star formation rate indicator (with all of its associated uncertainties). In addition, recent work finds a close re-

lationship between  $L_{12\mu\text{m}}$  and CO emission (e.g. Leroy et al. 2021; Gao et al. 2022) which further suggests that the *WISE* W3 band can be used as a powerful tracer of the ISM for galaxies distributed across the whole sky.

#### 5. SUMMARY AND CONCLUSIONS

We have carefully measured the *WISE* properties of galaxies in the extended S<sup>4</sup>G sample, which constitutes a powerful laboratory with which to examine the dust properties of nearby galaxies. We summarise our key results here:

1. Examining the relationship between *WISE* color and morphology we find that spheroids largely separate from disk galaxies in W1–W3 color, except for S0 and S0/a galaxies which can span the full range of W1–W3 color.
2. The distribution of S<sup>4</sup>G-*WISE* galaxies in W3–W4 color shows a tail towards redder *WISE* color indicative of a steep warm dust spectrum or, alternatively, a relative paucity of  $12\mu\text{m}$  emission.
3. Taking into account these “warm” sources (using the ratio of  $L_{12\mu\text{m}}$  to  $L_{23\mu\text{m}}$ ), we derive new relationships for W3 and W4 with  $L_{\text{TIR}}$ , which results in closer statistical agreement between  $\text{SFR}_{12\mu\text{m}}$  and  $\text{SFR}_{23\mu\text{m}}$ .
4. Using dust density ( $\Sigma_{12\mu\text{m}}$  in units of  $L_{\odot}/\text{kpc}^2$ ), we derive estimates of the  $\text{SFR}_{\text{deficit}}$  expected for low mass ( $\log M_{\text{stellar}} < 9.9 M_{\odot}$ ), low dust systems. This can be used to correct *WISE*-derived SFRs in this regime.
5. We investigate the ratio of mid-infrared emission to  $L_{\text{FUV}}$  for different morphological types, finding that  $L_{12\mu\text{m}}/L_{\text{FUV}}$  is well-correlated for Sc galaxies as a function of both  $M_{\text{stellar}}$  and  $\Sigma_{12\mu\text{m}}$ , but with increasing scatter for progressively earlier morphological types.
6. We use the weighted combination of  $\text{SFR}_{12\mu\text{m},\text{corr}}$  and  $\text{SFR}_{23\mu\text{m},\text{corr}}$  ( $\text{SFR}_{\text{MIR},\text{corr}}$ ) to investigate the location of different morphological types in the SFR- $M_{\text{stellar}}$  plane. This shows that galaxies with more prominent bulges are less likely to fall on the SFMS, and that Sc and Sd galaxies lie almost exclusively on the SFMS (as long as star formation is detected).

In conclusion, nearly 15 years since its launch, the *WISE* mission continues to build its legacy in the study of galaxies in the local Universe thanks to its combination of mid-infrared bands and all-sky coverage.

Star Formation (SF) Classification by Morphological Type					
Class	T-Type	Total	SF	Below SF	SF
		Galaxies	Sequence	Sequence	Not Detected
E	-5.0–-3.5	169	13.0%	48.5%	38.5%
E/S0	-3.5–-2.5	102	30.4%	39.2%	30.4%
S0	-2.5–-1.5	232	28.9%	44.4%	26.7%
S0/a	-1.5–0.5	206	58.7%	25.9%	12.1%
Sa	0.5–2.5	207	84.5%	14.5%	1.0%
Sb	2.5–4.5	412	99.5%	0.2%	0.2%
Sc	4.5–7.5	810	97.2%	0%	2.8%
Sd	7.5–8.5	171	91.2%	0%	8.8%

**Table 1.** The Star Formation Classification per morphological type (T-Type); see Fig.16 for the S<sup>4</sup>G sample. The number of galaxies where star formation was not detected ( $L_{12\mu m}$  upper limits) is given in the final column.

The authors would like to acknowledge the tragic passing of co-author, Dr Thomas Jarrett. We will continue your legacy, Tom, but we do so with heavy hearts. We thank the referee for recommendations that improved the content of this paper. MEC acknowledges the support of an Australian Research Council Future Fellowship (Project No. FT170100273) funded by the Australian Government. T.H.J. acknowledges support from the National Research Foundation (South Africa). This publication makes use of data products from the Wide-field Infrared Survey Explorer, which is a joint project of the University of California, Los Angeles, and the Jet Propulsion Laboratory/California Institute of Technology (JPL/Caltech), and NEOWISE, which is a project

of the JPL/Caltech. WISE and NEOWISE are funded by the National Aeronautics and Space Administration (NASA). This research has made use of the NASA/IPAC Extragalactic Database (NED) and the NASA/IPAC Infrared Science Archive (IRSA), which is operated by the JPL, Caltech, under contract with NASA.

*Facilities:* WISE, Spitzer, GALEX, NED, IRSA

*Software:* `astropy` (Astropy Collaboration et al. 2013, 2018), `matplotlib` (Hunter 2007), `NumPy` (van der Walt et al. 2011), and `SciPy` (Virtanen et al. 2020).

## APPENDIX

### A. THE SINGS/KINGFISH SAMPLE

As in Cluver et al. (2017), we make use of the combined SINGS (Kennicutt et al. 2003) and KINGFISH samples (Kennicutt et al. 2011) for our primary relations between  $L_{12\mu m}$  and  $L_{23\mu m}$ , and  $L_{TIR}$ . In total, we have measurements for 76 galaxies (the full SINGS/KINGFISH sample less HoI, HoII, and HoIX which are too faint and diffuse to be measured in *WISE*). Of these, 6 have upper limits for  $L_{12\mu m}$  and 3 have upper limits for  $L_{23\mu m}$  and are not included in the analysis that follows. Upper limits can result from either emission being too faint for reliable measurement (a non-detection) or, alternatively, due to stellar continuum emission dominating the signal in W3 and W4 which after removal results in a low confidence measurement. Photometry and derived properties for the SINGSFISH sample are included in Tables 3 and 4, respectively.

In Figure 17a we plot the W1–W2 versus W1–W3 colors for the SINGS/KINGFISH sample, separating sources with high  $\log(L_{12\mu m}/L_{23\mu m})$  ( $\geq -0.1$ ; black points) and low  $\log(L_{12\mu m}/L_{23\mu m})$  ( $< -0.1$ ; red points). NGC 1377 is colored green since it has very warm W1–W2 colors and would be classified as an AGN by that criterion (this source is therefore not included in the fits that follow). We note that this galaxy is not typical and has been identified as a nascent starburst (Roussel et al. 2006). The galaxy with elevated W1–W2 color which falls just below our delineation for AGN activity is NGC 1266, which is thought to harbor an obscured AGN (Alatalo et al. 2011). Galaxies with low S/N measurements ( $S/N < 5$ ) are shown in blue and also not included in any fits.

The W3–W4 colour distribution for the  $\log(L_{12\mu m}/L_{23\mu m}) \geq -0.1$  sources (black open histogram) and  $\log(L_{12\mu m}/L_{23\mu m}) < -0.1$  sources (red filled histogram) are shown in Figure 17. Given the small sample size, the division appears contrived, but a significant number of the SINGS/KINGFISH sources fall into this category.

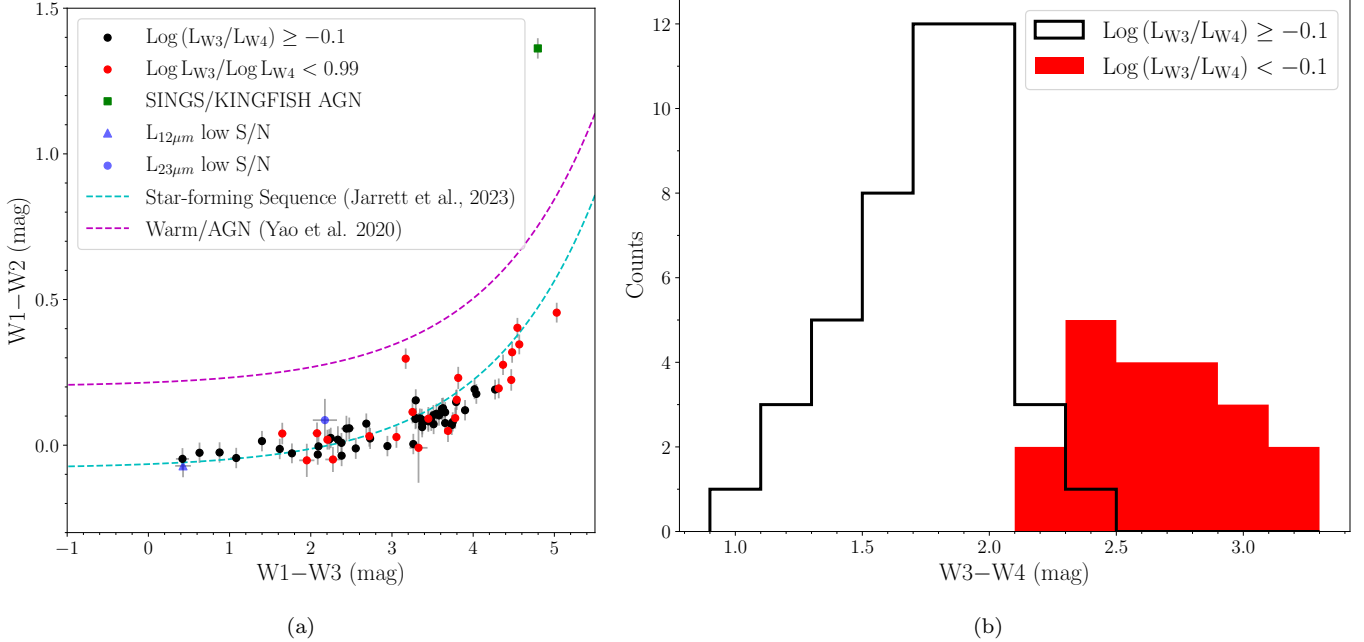


**Figure 17.** (a) The SINGS/KINGFISH *WISE* color-color diagram showing the color distribution  $\log(L_{12\mu m}/L_{23\mu m}) \geq -0.1$  sources (black points) and  $\log(L_{12\mu m}/L_{23\mu m}) < -0.1$  sources (red points). The green point is NGC 1377 while the red outlier with elevated  $W1-W2$  is NGC 1266. (b) Histogram of the  $W3-W4$  colors of the SINGS/KINGFISH sources separated by  $\log(L_{12\mu m}/L_{23\mu m}) \geq -0.1$  or  $< -0.1$ . The much smaller sample size compared to  $S^4G$  makes it more difficult to see a separation between their distributions (compared to Figure 6).

We next re-examine the relationships derived in Cluver et al. (2017) taking advantage of improved measurements and more robust and internally consistent adopted distances. The correspondence between  $\log L_{TIR}$  and  $\log L_{12\mu m}$  is shown in Figure 18a; we see little difference in the behaviour of the red and black sources (although most of the low luminosity sources have “warm” mid-infrared colours relatively high  $L_{23\mu m}$  compared to  $L_{12\mu m}$ ). The fit to all sources is given by:

$$\log L_{TIR}(L_{\odot}) = 0.886(\pm 0.022) \log L_{12\mu m}(L_{\odot}) + 2.04(\pm 0.20) \quad (A1)$$

with a  $1\sigma$  scatter of 0.10 dex.

However, when we examine the relationship between  $L_{TIR}$  and  $L_{23\mu m}$  in Figure 18b, we find the  $\log(L_{12\mu m}/L_{23\mu m}) < -0.1$  sources (red points) appear systematically offset from the black points. Comparing the slopes of the fits to the black and red points, respectively, we see that they are very similar and we are therefore observing a shift to higher  $L_{23\mu m}$  relative to  $L_{TIR}$ . The best fit relations are given by:

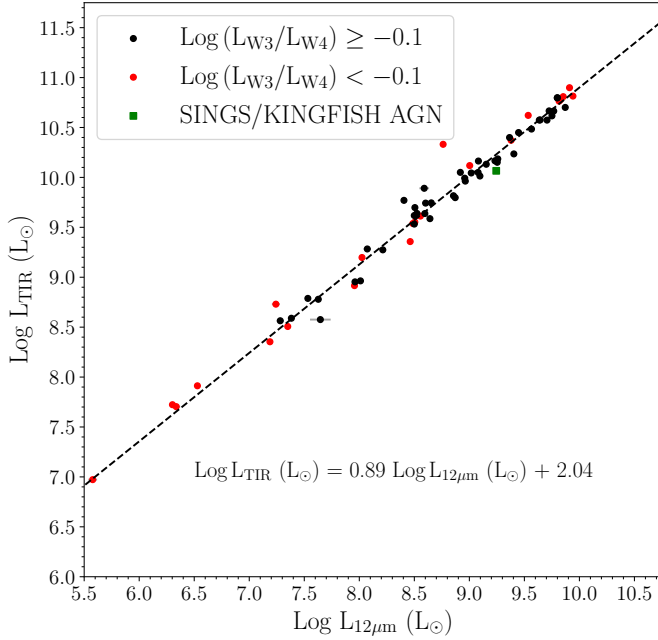
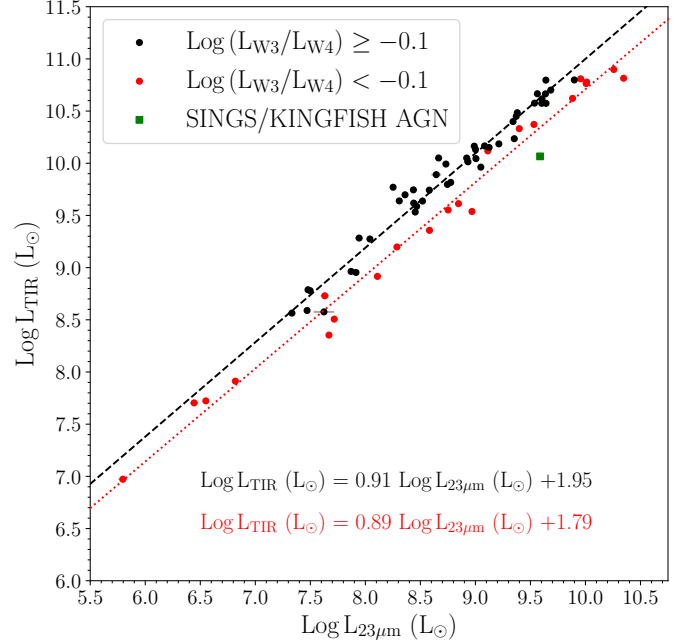
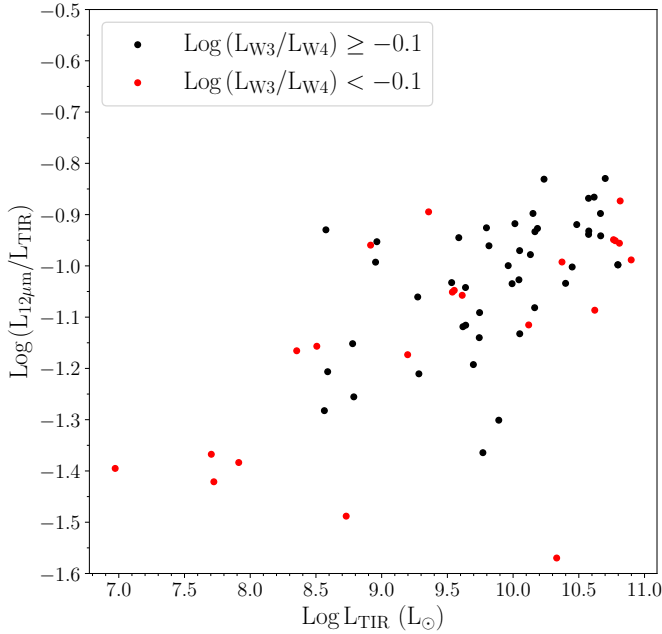
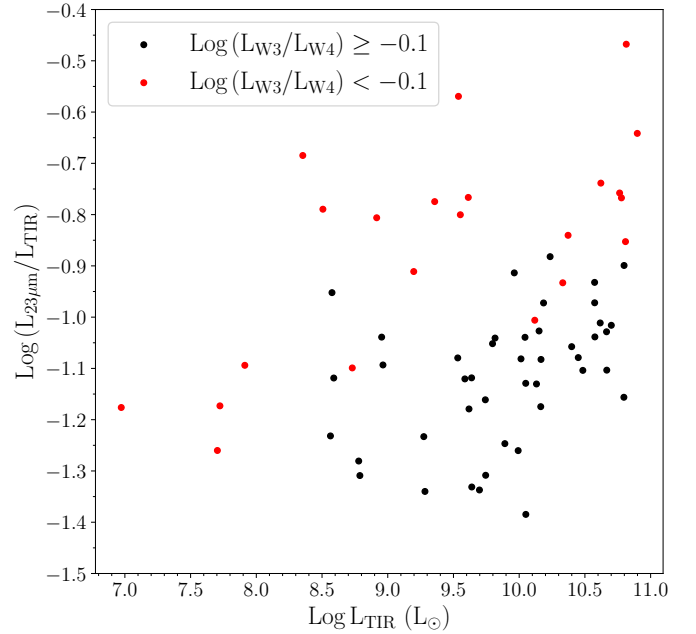
$$\log L_{TIR}(L_{\odot}) = 0.91(\pm 0.03) \log L_{23\mu m}(L_{\odot}) + 1.95(\pm 0.23) \quad (A2)$$

with a  $1\sigma$  scatter of 0.12 dex for “nominal” mid-infrared sources (i.e.  $\log(L_{12\mu m}/L_{23\mu m}) \geq -0.1$ , and,

$$\log L_{TIR}(L_{\odot}) = 0.89(\pm 0.02) \log L_{23\mu m}(L_{\odot}) + 1.79(\pm 0.19) \quad (A3)$$

with a  $1\sigma$  scatter of 0.14 dex for “warm” mid-infrared sources (i.e.  $\log(L_{12\mu m}/L_{23\mu m}) < -0.1$ ). We note that in Cluver et al. (2017) the  $1\sigma$  scatter of the  $L_{23\mu m} - L_{TIR}$  relation (i.e. without making a distinction based on mid-IR color) was 0.18 dex.

We more closely examine the behaviour of  $L_{12\mu m}$  and  $L_{23\mu m}$  relative to  $L_{TIR}$  in Figure 18c and d, respectively. For “nominal” sources (black points) we see that  $L_{12\mu m}$  and  $L_{23\mu m}$  track  $L_{TIR}$  very similarly for  $L_{TIR} > 8.5 L_{\odot}$ . However, we see that “warm” mid-IR sources (red points) at lower  $L_{TIR}$  show more of a deficit at  $L_{12\mu m}$  compared to  $L_{23\mu m}$ , but appear well-mixed with the nominal  $W3-W4$  color sources (black points) for  $L_{TIR} > 8.5 L_{\odot}$ . On the other hand,

(a)  $\text{Log } L_{\text{TIR}}$  vs.  $\text{Log } L_{12\mu\text{m}}$ (b)  $\text{Log } L_{\text{TIR}}$  vs.  $\text{Log } L_{23\mu\text{m}}$ (c)  $\text{Log } L_{12\mu\text{m}}/\text{Log } L_{\text{TIR}}$  vs.  $\text{Log } L_{\text{TIR}}$ (d)  $\text{Log } L_{23\mu\text{m}}/\text{Log } L_{\text{TIR}}$  vs.  $\text{Log } L_{\text{TIR}}$ 

**Figure 18.** The relationship between  $\text{Log } L_{12\mu\text{m}}$ ,  $\text{Log } L_{23\mu\text{m}}$  and  $\text{Log } L_{\text{TIR}}$  with sources separated by  $L_{12\mu\text{m}}/L_{23\mu\text{m}}$  ratio.

the red sources at higher  $L_{\text{TIR}}$  are systematically higher than the nominal W3–W4 color sources. This behaviour is what drives the shift to the right in the relation seen in Figure 18b. We defer a more detailed examination of the properties of these two populations to a future publication.

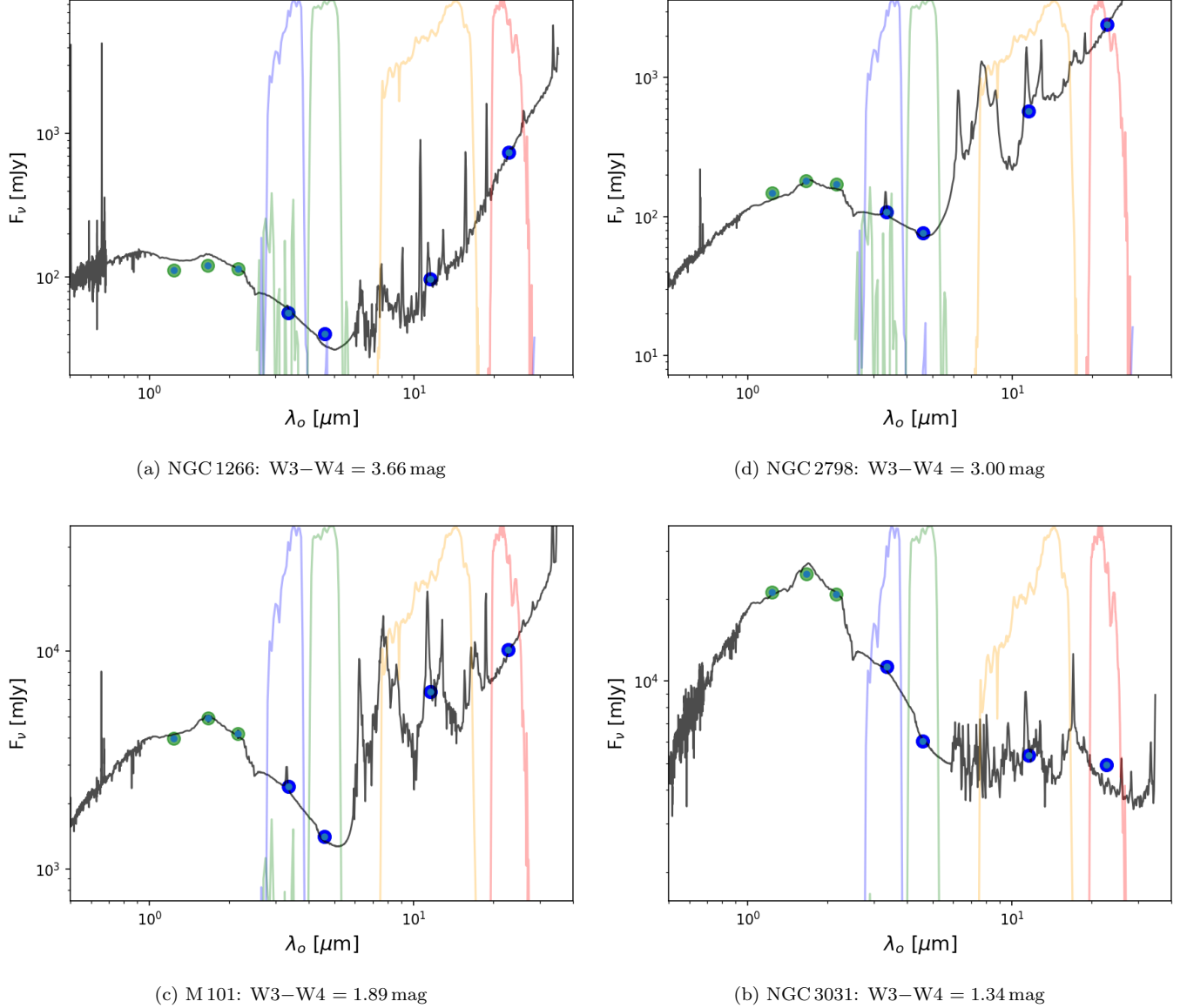


**Figure 19.** The Spectral Energy Distributions (SEDs) of selected sources illustrating the variation in  $W3-W4$  (see also Figure 6); details of the templates used and methodology followed can be found in Appendix A of Jarrett et al. (2023). The green points correspond to the  $J$ ,  $H$ , and  $K_s$  total fluxes from the 2MASS (Skrutskie et al. 2006) Extended Source Catalogues (XSC; Jarrett et al. 2003), while the blue points correspond to  $W1$ ,  $W2$ ,  $W3$  and  $W4$  bands, respectively. The filter response functions of the four *WISE* bands (Jarrett et al. 2011) are also shown.

## B. SELECTED SEDS

In Figure 19 we include the spectral energy distributions of four large galaxies to illustrate the variation in  $W3-W4$  color due to star formation and nuclear activity. The galaxies are: NGC 1266 (a lenticular galaxy hosting a Seyfert nucleus), NGC 2798 (an SBa type undergoing tidal interaction and likely starburst), M 101 (an Scd galaxy and classic face-on grand-design spiral) and M 81/NGC 3031 (classified as Sab).

## C. HYBRID SFR COMPARISONS

In this section we compare  $\text{SFR}_{12\mu\text{m,corr}}$  to selected hybrid FUV+W4 SFR indicators from the literature. Since  $\text{SFR}_{12\mu\text{m,corr}}$  and  $\text{SFR}_{23\mu\text{m,corr}}$  are calibrated to be consistent with each other, this also reflects the overall performance of  $\text{SFR}_{23\mu\text{m,corr}}$ , but without the complexity of comparing two indicators that both rely on W4.

In Figure 20a we compare to the FUV+W4 relation of [Belfiore et al. \(2023\)](#), and in panel (b) to the FUV+W4 relation [Leroy et al. \(2019\)](#). In panel (c) we compare to the FUV+24  $\mu\text{m}$  relation of [Boquien et al. \(2016\)](#), derived using Spitzer MIPS, and in panel (d) to the FUV+25  $\mu\text{m}$  relation of [Hao et al. \(2011\)](#) derived using IRAS 25  $\mu\text{m}$  measurements. For the latter two relations we convert our W4 measurement to a proxy MIPS 24  $\mu\text{m}$  flux using templates from the GRASIL code ([Silva et al. 1998b](#)) for different morphological types (a factor of 1.1 is appropriate to convert 22.8  $\mu\text{m}$  W4 to an approximate 23.675  $\mu\text{m}$  MIPS measurement for S0 to Sd galaxy types). We treat the proxy MIPS 24  $\mu\text{m}$  measurement as representative of the equivalent IRAS 25  $\mu\text{m}$  value for the purposes of this comparison. We note that [Boquien et al. \(2016\)](#) provide FUV–3.6  $\mu\text{m}$  color limits to remove spurious and unphysical measurements; we apply these as FUV–W1 color cuts for all sources shown in Figure 20.

Overall we see good agreement with [Belfiore et al. \(2023\)](#), albeit with large scatter, and with [Leroy et al. \(2019\)](#) and [Hao et al. \(2011\)](#). We see an offset and SFR dependence when comparing to [Boquien et al. \(2016\)](#) (Figure 20c), which is also seen (and discussed) in [Belfiore et al. \(2023\)](#).

All 4 panels of Figure 20 show a clump of sources to the bottom left which imply a large  $\text{SFR}_{12\mu\text{m,corr}}$  compared to the hybrid FUV+MIR derived value. We select all sources with  $\text{Log SFR}_{\text{FUV+W4}} (\text{B23}) - \text{Log SFR}_{12\mu\text{m,corr}} < -0.5$ , since this captures the largest population that show this offset, and examine their properties further in Figure 21.

Figure 21a shows the ratio of  $L_{23\mu\text{m}}$  to  $L_{\text{FUV}}$  as a function of  $L_{12\mu\text{m}}$ , with the outliers from Figure C shown as red points. We see that these lie above the track inhabited by the other sources in the sample; to further understand this we show the same ratio as a function of  $L_{\text{FUV}}$  in Figure 21b. This suggests that these sources have a relative paucity of FUV emission which shifts the  $L_{23\mu\text{m}}/L_{\text{FUV}}$  ratio to higher values. In order to investigate the possibility that the  $L_{23\mu\text{m}}$  is elevated compared to  $L_{12\mu\text{m}}$ , thus causing a higher  $L_{23\mu\text{m}}/L_{\text{FUV}}$  ratio, we examine the  $L_{12\mu\text{m}}/L_{23\mu\text{m}}$  ratio as a function of  $L_{23\mu\text{m}}$  in Figure 21c. Here we see that the majority of sources have typical  $L_{12\mu\text{m}}$  to  $L_{23\mu\text{m}}$  values, which further suggests that the FUV emission for the outliers is low compared to both  $L_{12\mu\text{m}}$  and  $L_{23\mu\text{m}}$ . Since we are comparing  $\text{SFR}_{12\mu\text{m,corr}}$  to  $\text{SFR}_{\text{FUV+W4}}$ , it is important to check that this is not induced by applying the correction as discussed in Section 3.2.2. In Figure 21d we plot the  $L_{23\mu\text{m}}/L_{\text{FUV}}$  ratio as a function of  $M_{\text{stellar}}$ , which shows that these sources are found across the stellar mass range of the sample and the majority are found in a mass range where the  $\text{SFR}_{12\mu\text{m}}$  deficit correction is negligibly small or irrelevant.

## D. IRX MORPHOLOGY PLOTS

In Figure 11 we showed the  $\log(L_{12\mu\text{m}}/L_{\text{FUV}})$  as a function of  $\log \Sigma_{12\mu\text{m}}$  for galaxies with masses  $\log M_{\text{stellar}} < 9.9 M_{\odot}$ . We include here the  $\log(L_{12\mu\text{m}}/L_{\text{FUV}})$  values as a function of  $\log \Sigma_{12\mu\text{m}}$  (Figure 22) and  $\log(L_{23\mu\text{m}}/L_{\text{FUV}})$  values as a function of  $\log \Sigma_{23\mu\text{m}}$  (Figure 23) for the full sample (first panel) and separated by morphological type in the subsequent panels. The fit to the Sc galaxies is given by:

$$\text{Log}(L_{12\mu\text{m}}/L_{\text{FUV}}) = 1.24 \log \Sigma_{12\mu\text{m}} - 8.39, \quad (\text{D4})$$

in Figure 22 and

$$\text{Log}(L_{23\mu\text{m}}/L_{\text{FUV}}) = 1.02 \log \Sigma_{23\mu\text{m}} - 7.11, \quad (\text{D5})$$

in Figure 23 (reproduced in each panel (as the grey line)). Galaxies with  $\log M_{\text{stellar}} > 10.5 M_{\odot}$  are shown as silver points in each panel.

The distribution of points in both figures is similar, albeit with more scatter in Figure 23 (consistent with what is seen in Figure 11). Galaxies with  $\log M_{\text{stellar}} > 10.5 M_{\odot}$  do not appear to be noticeably different in their distribution compared to lower mass galaxies, but there appears to be a trend with morphology where earlier types tend to show elevated  $L_{12\mu\text{m}}/L_{\text{FUV}}$  and  $L_{23\mu\text{m}}/L_{\text{FUV}}$ , respectively. This suggests decreased  $L_{\text{FUV}}$  relative to  $L_{12\mu\text{m}}$  and  $L_{23\mu\text{m}}$  and may be the result of increased dust not associated with recent star formation; this is particularly noticeable in the E/S0/S0-a panel.

## REFERENCES

- Alatalo, K., Blitz, L., Young, L. M., et al. 2011, *ApJ*, 735, 88, doi: [10.1088/0004-637X/735/2/88](https://doi.org/10.1088/0004-637X/735/2/88)
- Astropy Collaboration, Robitaille, T. P., Tollerud, E. J., et al. 2013, *A&A*, 558, A33, doi: [10.1051/0004-6361/201322068](https://doi.org/10.1051/0004-6361/201322068)

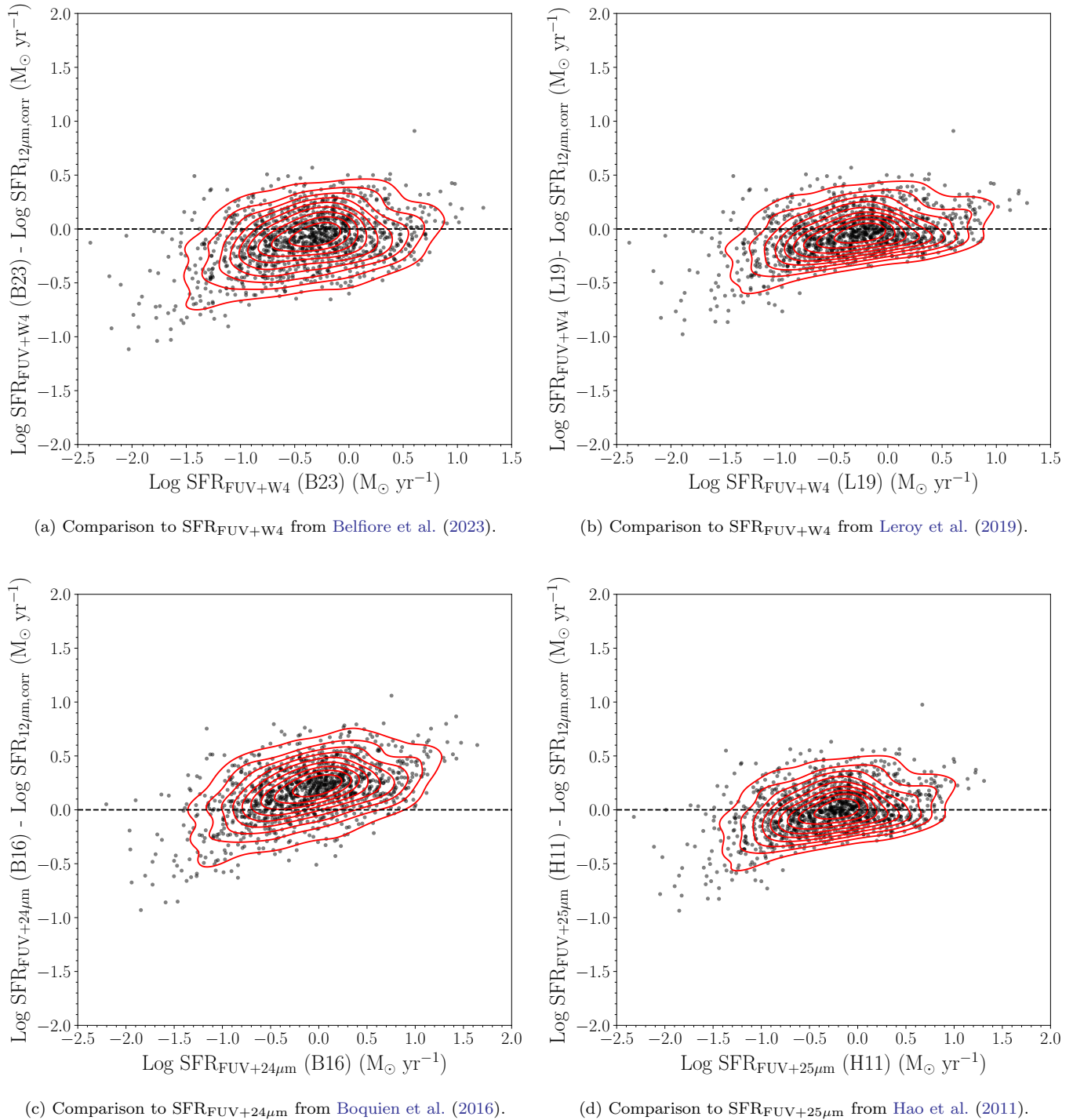


**Figure 20.** A comparison between corrected  $12\mu\text{m}$ -derived SFRs (Equation 7) and hybrid UV+IR SFR relations from the literature show overall consistency and broad agreement; outliers from panel (a) are examined in the next figure.

Astropy Collaboration, Price-Whelan, A. M., Sipőcz, B. M., et al. 2018, *AJ*, 156, 123, doi: [10.3847/1538-3881/aabc4f](https://doi.org/10.3847/1538-3881/aabc4f)

Baes, M., Verstappen, J., De Looze, I., et al. 2011, *ApJS*, 196, 22, doi: [10.1088/0067-0049/196/2/22](https://doi.org/10.1088/0067-0049/196/2/22)

Belfiore, F., Leroy, A. K., Williams, T. G., et al. 2023, *A&A*, 678, A129, doi: [10.1051/0004-6361/202347175](https://doi.org/10.1051/0004-6361/202347175)

Bok, J., Skelton, R. E., Cluver, M. E., et al. 2020, *MNRAS*, 499, 3193, doi: [10.1093/mnras/staa3034](https://doi.org/10.1093/mnras/staa3034)

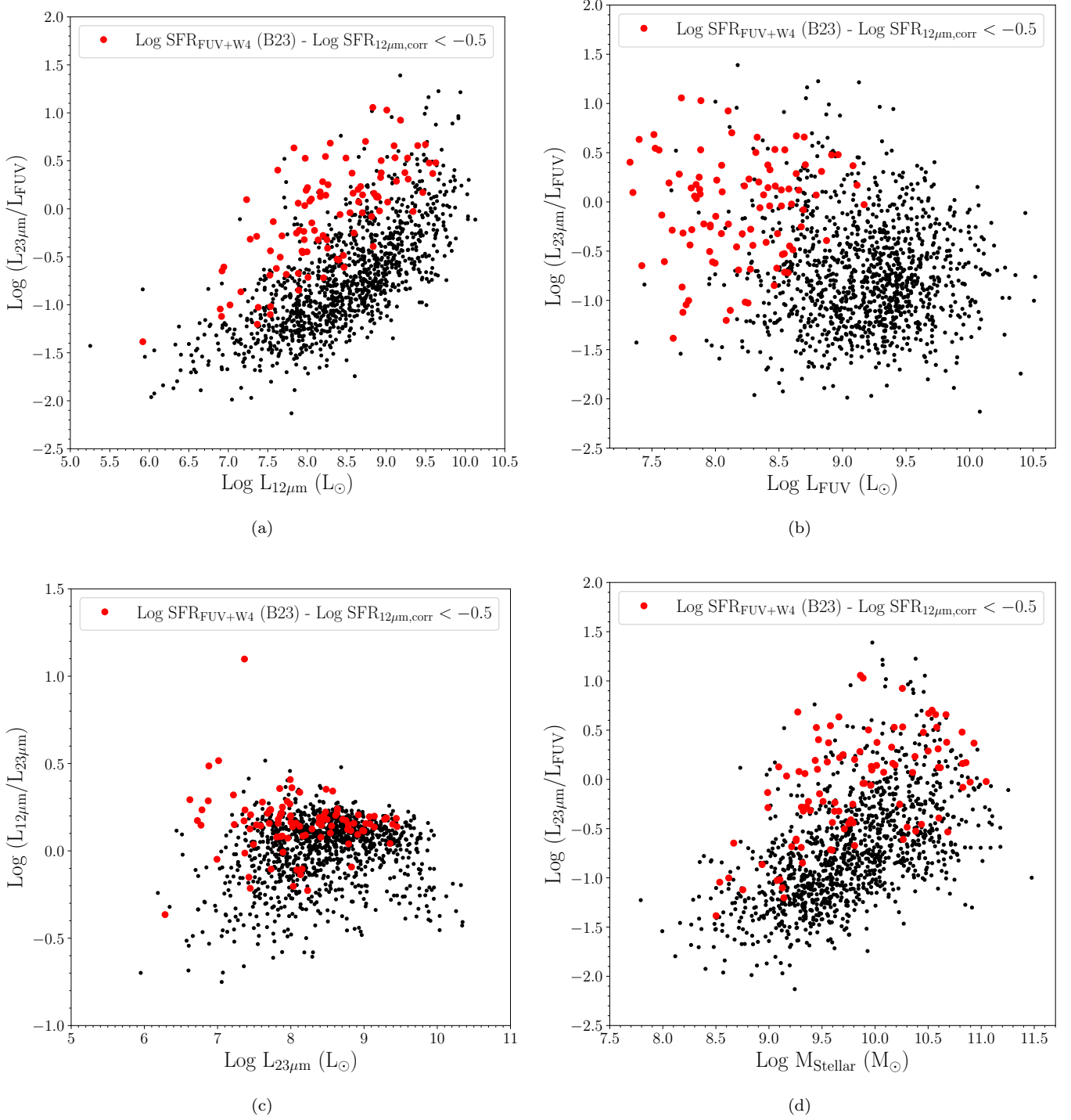


**Figure 21.** Investigating the outliers from Figure C (red points) compared to the ensemble (black points) by considering the ratio of  $L_{23\mu\text{m}}$  to  $L_{\text{FUV}}$  and  $L_{12\mu\text{m}}$  to  $L_{\text{FUV}}$  as a function of  $L_{12\mu\text{m}}$ ,  $L_{23\mu\text{m}}$ ,  $L_{\text{FUV}}$  and  $M_{\text{stellar}}$ . We see that the red points do not show a stellar mass dependence, but do appear to be associated with relatively low levels of UV emission relative to mid-IR dust emission.

Boquien, M., Burgarella, D., Roehlly, Y., et al. 2019, A&A,

622, A103, doi: [10.1051/0004-6361/201834156](https://doi.org/10.1051/0004-6361/201834156)

Boquien, M., Kennicutt, R., Calzetti, D., et al. 2016, A&A,

591, A6, doi: [10.1051/0004-6361/201527759](https://doi.org/10.1051/0004-6361/201527759)

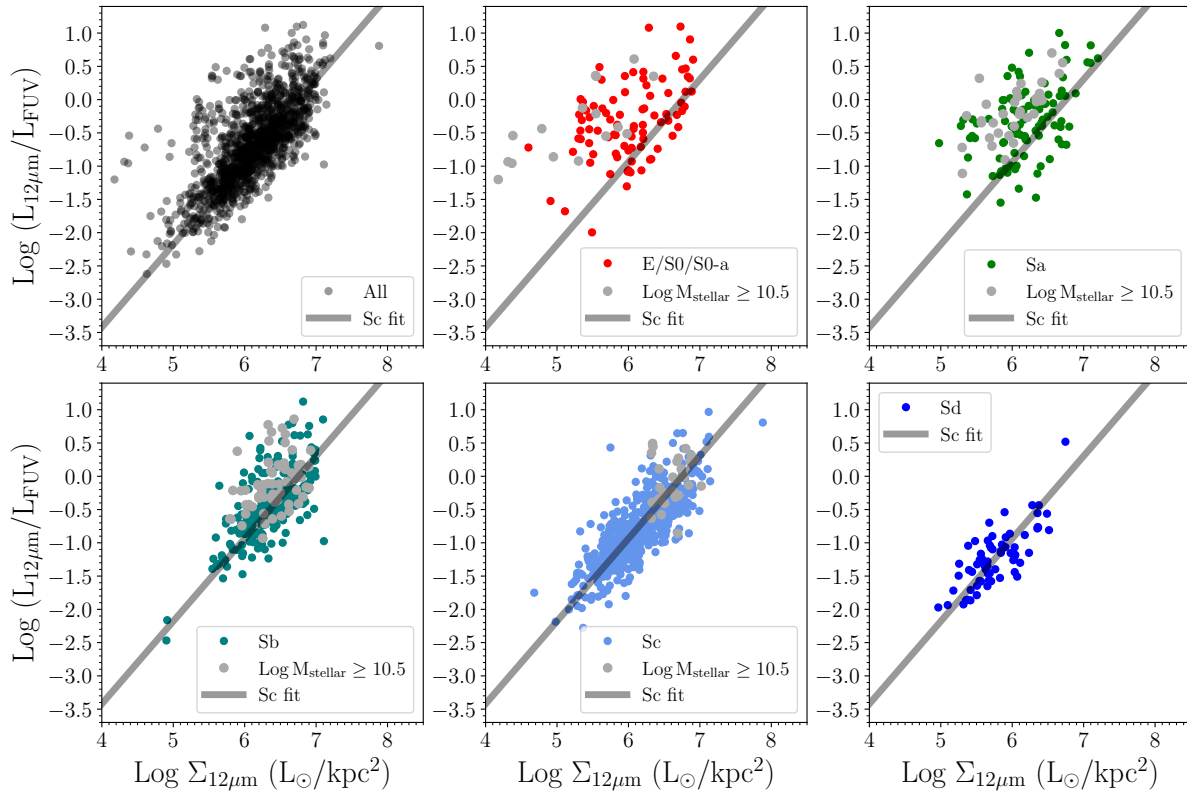


**Figure 22.** The  $\log(L_{12\mu\text{m}}/L_{\text{FUV}})$  versus  $\log \Sigma_{12\mu\text{m}}$  for the whole  $S^4G$ -*WISE* UV sample (first panel) and separated by morphology. Galaxies with  $\log M_{\text{stellar}} > 10.5 M_{\odot}$  are highlighted as silver points. The fit to sources in the Sc panel (light blue points) is shown in each panel (as the grey line). This figure is complementary to Figure 12 showing the same panels as a function of  $M_{\text{stellar}}$ .

Bouquin, A. Y. K., Gil de Paz, A., Muñoz-Mateos, J. C., et al. 2018, *ApJS*, 234, 18, doi: [10.3847/1538-4365/aaa384](https://doi.org/10.3847/1538-4365/aaa384)

Bouwens, R. J., Aravena, M., Decarli, R., et al. 2016, *ApJ*, 833, 72, doi: [10.3847/1538-4357/833/1/72](https://doi.org/10.3847/1538-4357/833/1/72)

Brown, M. J. I., Moustakas, J., Smith, J. D. T., et al. 2014, *ApJS*, 212, 18, doi: [10.1088/0067-0049/212/2/18](https://doi.org/10.1088/0067-0049/212/2/18)

Calzetti, D. 2013, in *Secular Evolution of Galaxies*, ed. J. Falcón-Barroso & J. H. Knapen, 419, doi: [10.48550/arXiv.1208.2997](https://doi.org/10.48550/arXiv.1208.2997)

Calzetti, D., Adamo, A., Linden, S. T., et al. 2024, arXiv e-prints, arXiv:2406.01831, doi: [10.48550/arXiv.2406.01831](https://doi.org/10.48550/arXiv.2406.01831)

Cardelli, J. A., Clayton, G. C., & Mathis, J. S. 1989, *ApJ*, 345, 245, doi: [10.1086/167900](https://doi.org/10.1086/167900)

Chabrier, G. 2003, *PASP*, 115, 763, doi: [10.1086/376392](https://doi.org/10.1086/376392)

Chevallard, J., & Charlot, S. 2016, *MNRAS*, 462, 1415, doi: [10.1093/mnras/stw1756](https://doi.org/10.1093/mnras/stw1756)

Cluver, M. E., Jarrett, T. H., Dale, D. A., et al. 2017, *ApJ*, 850, 68, doi: [10.3847/1538-4357/aa92c7](https://doi.org/10.3847/1538-4357/aa92c7)

Cluver, M. E., Jarrett, T. H., Taylor, E. N., et al. 2020, *ApJ*, 898, 20, doi: [10.3847/1538-4357/ab9cb8](https://doi.org/10.3847/1538-4357/ab9cb8)

Cutri, R. M., Wright, E. L., Conrow, T., et al. 2012, Explanatory Supplement to the WISE All-Sky Data Release Products, Explanatory Supplement to the WISE All-Sky Data Release Products

da Cunha, E., Charlot, S., & Elbaz, D. 2008, *MNRAS*, 388, 1595, doi: [10.1111/j.1365-2966.2008.13535.x](https://doi.org/10.1111/j.1365-2966.2008.13535.x)

Dale, D. A., & Helou, G. 2002, *ApJ*, 576, 159, doi: [10.1086/341632](https://doi.org/10.1086/341632)

Dale, D. A., Helou, G., Contursi, A., Silbermann, N. A., & Kolhatkar, S. 2001, *The Astrophysical Journal*, 549, 215, doi: [10.1086/319077](https://doi.org/10.1086/319077)

Dale, D. A., Helou, G., Magdis, G. E., et al. 2014, *ApJ*, 784, 83, doi: [10.1088/0004-637X/784/1/83](https://doi.org/10.1088/0004-637X/784/1/83)

Dale, D. A., Gil de Paz, A., Gordon, K. D., et al. 2007, *ApJ*, 655, 863, doi: [10.1086/510362](https://doi.org/10.1086/510362)

Dale, D. A., Cook, D. O., Roussel, H., et al. 2017, *ApJ*, 837, 90, doi: [10.3847/1538-4357/aa6032](https://doi.org/10.3847/1538-4357/aa6032)

Davies, J. I., Baes, M., Bianchi, S., et al. 2017, *PASP*, 129, 044102, doi: [10.1088/1538-3873/129/974/044102](https://doi.org/10.1088/1538-3873/129/974/044102)

Davies, L. J. M., Driver, S. P., Robotham, A. S. G., et al. 2016, *MNRAS*, 461, 458, doi: [10.1093/mnras/stw1342](https://doi.org/10.1093/mnras/stw1342)

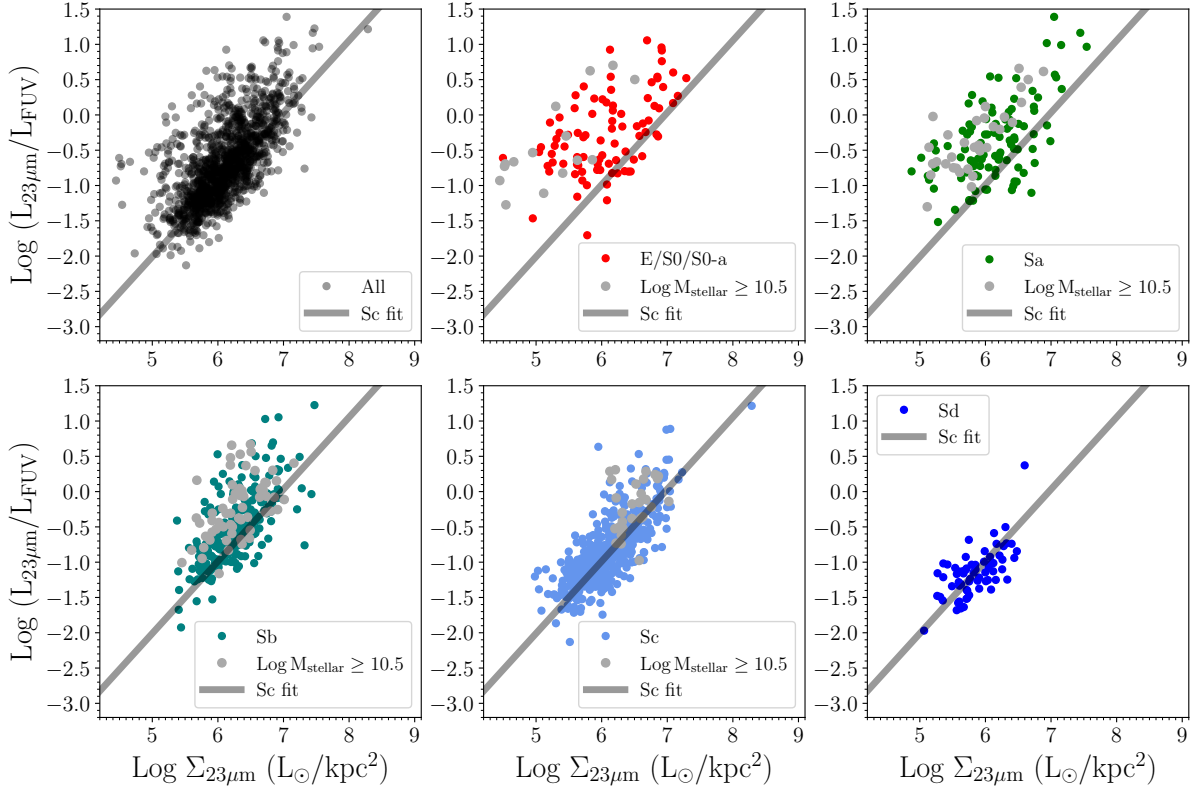


**Figure 23.** Same as in Figure 22, but for  $\log(L_{23\mu m}/L_{FUV})$  as a function of  $\log \Sigma_{23\mu m}$ .

- de Jong, R. S., Agertz, O., Berbel, A. A., et al. 2019, *The Messenger*, 175, 3, doi: [10.18727/0722-6691/5117](https://doi.org/10.18727/0722-6691/5117)
- De Looze, I., Fritz, J., Baes, M., et al. 2014, *A&A*, 571, A69, doi: [10.1051/0004-6361/201424747](https://doi.org/10.1051/0004-6361/201424747)
- Draine, B. T., Li, A., Hensley, B. S., et al. 2021, *ApJ*, 917, 3, doi: [10.3847/1538-4357/abff51](https://doi.org/10.3847/1538-4357/abff51)
- Draine, B. T., Aniano, G., Krause, O., et al. 2014, *ApJ*, 780, 172, doi: [10.1088/0004-637X/780/2/172](https://doi.org/10.1088/0004-637X/780/2/172)
- Gao, Y., Tan, Q.-H., Gao, Y., et al. 2022, *ApJ*, 940, 133, doi: [10.3847/1538-4357/ac9af1](https://doi.org/10.3847/1538-4357/ac9af1)
- Goovaerts, I., Pello, R., Burgarella, D., et al. 2024, *A&A*, 683, A184, doi: [10.1051/0004-6361/202348011](https://doi.org/10.1051/0004-6361/202348011)
- Hao, C.-N., Kennicutt, R. C., Johnson, B. D., et al. 2011, *ApJ*, 741, 124, doi: [10.1088/0004-637X/741/2/124](https://doi.org/10.1088/0004-637X/741/2/124)
- Helou, G. 1986, *ApJL*, 311, L33, doi: [10.1086/184793](https://doi.org/10.1086/184793)
- Houston, T., Croton, D. J., & Sinha, M. 2023, *MNRAS*, 522, L11, doi: [10.1093/mnras/slad031](https://doi.org/10.1093/mnras/slad031)
- Huchra, J. P., Macri, L. M., Masters, K. L., et al. 2012, *ApJS*, 199, 26, doi: [10.1088/0067-0049/199/2/26](https://doi.org/10.1088/0067-0049/199/2/26)
- Hunt, L. K., De Looze, I., Boquien, M., et al. 2019, *A&A*, 621, A51, doi: [10.1051/0004-6361/201834212](https://doi.org/10.1051/0004-6361/201834212)
- Hunter, J. D. 2007, *Computing in Science and Engineering*, 9, 90, doi: [10.1109/MCSE.2007.55](https://doi.org/10.1109/MCSE.2007.55)
- Ivezić, Ž., Kahn, S. M., Tyson, J. A., et al. 2019, *ApJ*, 873, 111, doi: [10.3847/1538-4357/ab042c](https://doi.org/10.3847/1538-4357/ab042c)
- Jarrett, T. H., Chester, T., Cutri, R., Schneider, S. E., & Huchra, J. P. 2003, *AJ*, 125, 525, doi: [10.1086/345794](https://doi.org/10.1086/345794)
- Jarrett, T. H., Cluver, M. E., Brown, M. J. I., et al. 2019, *ApJS*, 245, 25, doi: [10.3847/1538-4365/ab521a](https://doi.org/10.3847/1538-4365/ab521a)
- Jarrett, T. H., Cluver, M. E., Taylor, E. N., et al. 2023, *ApJ*, 946, 95, doi: [10.3847/1538-4357/acb68f](https://doi.org/10.3847/1538-4357/acb68f)
- Jarrett, T. H., Cohen, M., Masci, F., et al. 2011, *ApJ*, 735, 112, doi: [10.1088/0004-637X/735/2/112](https://doi.org/10.1088/0004-637X/735/2/112)
- Jarrett, T. H., Masci, F., Tsai, C. W., et al. 2012, *AJ*, 144, 68, doi: [10.1088/0004-6256/144/2/68](https://doi.org/10.1088/0004-6256/144/2/68)
- . 2013, *AJ*, 145, 6, doi: [10.1088/0004-6256/145/1/6](https://doi.org/10.1088/0004-6256/145/1/6)
- Kennicutt, Robert C., J. 1998, *ARA&A*, 36, 189, doi: [10.1146/annurev.astro.36.1.189](https://doi.org/10.1146/annurev.astro.36.1.189)
- Kennicutt, Robert C., J., Armus, L., Bendo, G., et al. 2003, *PASP*, 115, 928, doi: [10.1086/376941](https://doi.org/10.1086/376941)
- Kennicutt, R. C., & Evans, N. J. 2012, *ARA&A*, 50, 531, doi: [10.1146/annurev-astro-081811-125610](https://doi.org/10.1146/annurev-astro-081811-125610)
- Kennicutt, R. C., Calzetti, D., Aniano, G., et al. 2011, *PASP*, 123, 1347, doi: [10.1086/663818](https://doi.org/10.1086/663818)
- Kroupa, P. 2001, *MNRAS*, 322, 231, doi: [10.1046/j.1365-8711.2001.04022.x](https://doi.org/10.1046/j.1365-8711.2001.04022.x)

- Lai, T. S. Y., Armus, L., Bianchin, M., et al. 2023, *ApJL*, 957, L26, doi: [10.3847/2041-8213/ad0387](https://doi.org/10.3847/2041-8213/ad0387)
- Leitherer, C., Schaerer, D., Goldader, J. D., et al. 1999, *ApJS*, 123, 3, doi: [10.1086/313233](https://doi.org/10.1086/313233)
- Leja, J., Johnson, B. D., Conroy, C., van Dokkum, P. G., & Byler, N. 2017, *ApJ*, 837, 170, doi: [10.3847/1538-4357/aa5ffe](https://doi.org/10.3847/1538-4357/aa5ffe)
- Leroy, A. K., Sandstrom, K. M., Lang, D., et al. 2019, *ApJS*, 244, 24, doi: [10.3847/1538-4365/ab3925](https://doi.org/10.3847/1538-4365/ab3925)
- Leroy, A. K., Schinnerer, E., Hughes, A., et al. 2021, *ApJS*, 257, 43, doi: [10.3847/1538-4365/ac17f3](https://doi.org/10.3847/1538-4365/ac17f3)
- Li, Y. A., Ho, L. C., Shangguan, J., Zhuang, M.-Y., & Li, R. 2023, *ApJS*, 267, 17, doi: [10.3847/1538-4365/acd4b5](https://doi.org/10.3847/1538-4365/acd4b5)
- Lu, N., Helou, G., Werner, M. W., et al. 2003, *ApJ*, 588, 199, doi: [10.1086/374043](https://doi.org/10.1086/374043)
- Makarov, Dmitry, Prugniel, Philippe, Terekhova, Nataliya, Courtois, Hélène, & Vauglin, Isabelle. 2014, *A&A*, 570, A13, doi: [10.1051/0004-6361/201423496](https://doi.org/10.1051/0004-6361/201423496)
- Martin, D. C., Fanson, J., Schiminovich, D., et al. 2005, *ApJL*, 619, L1, doi: [10.1086/426387](https://doi.org/10.1086/426387)
- Meidt, S. E., Schinnerer, E., van de Ven, G., et al. 2014, *ApJ*, 788, 144, doi: [10.1088/0004-637X/788/2/144](https://doi.org/10.1088/0004-637X/788/2/144)
- Muñoz-Mateos, J. C., Sheth, K., Gil de Paz, A., et al. 2013, *ApJ*, 771, 59, doi: [10.1088/0004-637X/771/1/59](https://doi.org/10.1088/0004-637X/771/1/59)
- Nersesian, A., Xilouris, E. M., Bianchi, S., et al. 2019, *A&A*, 624, A80, doi: [10.1051/0004-6361/201935118](https://doi.org/10.1051/0004-6361/201935118)
- Noeske, K. G., Weiner, B. J., Faber, S. M., et al. 2007, *ApJL*, 660, L43, doi: [10.1086/517926](https://doi.org/10.1086/517926)
- Pacifici, C., Iyer, K. G., Mobasher, B., et al. 2023, *ApJ*, 944, 141, doi: [10.3847/1538-4357/acacff](https://doi.org/10.3847/1538-4357/acacff)
- Peek, J. E. G., & Schiminovich, D. 2013, *ApJ*, 771, 68, doi: [10.1088/0004-637X/771/1/68](https://doi.org/10.1088/0004-637X/771/1/68)
- Peltonen, J., Rosolowsky, E., Williams, T. G., et al. 2024, *MNRAS*, 527, 10668, doi: [10.1093/mnras/stad3879](https://doi.org/10.1093/mnras/stad3879)
- Polletta, M., Tاجر, M., Maraschi, L., et al. 2007, *ApJ*, 663, 81, doi: [10.1086/518113](https://doi.org/10.1086/518113)
- Polletta, M. d. C., Wilkes, B. J., Siana, B., et al. 2006, *ApJ*, 642, 673, doi: [10.1086/500821](https://doi.org/10.1086/500821)
- Popesso, P., Morselli, L., Concas, A., et al. 2019, *MNRAS*, 490, 5285, doi: [10.1093/mnras/stz2635](https://doi.org/10.1093/mnras/stz2635)
- Querejeta, M., Meidt, S. E., Schinnerer, E., et al. 2015, *ApJS*, 219, 5, doi: [10.1088/0067-0049/219/1/5](https://doi.org/10.1088/0067-0049/219/1/5)
- Renzini, A., & Peng, Y.-j. 2015, *ApJL*, 801, L29, doi: [10.1088/2041-8205/801/2/L29](https://doi.org/10.1088/2041-8205/801/2/L29)
- Robotham, A. S. G., Bellstedt, S., Lagos, C. d. P., et al. 2020, *MNRAS*, 495, 905, doi: [10.1093/mnras/staa1116](https://doi.org/10.1093/mnras/staa1116)
- Robotham, A. S. G., & Obreschkow, D. 2015, *PASA*, 32, e033, doi: [10.1017/pasa.2015.33](https://doi.org/10.1017/pasa.2015.33)
- Roussel, H., Helou, G., Smith, J. D., et al. 2006, *ApJ*, 646, 841, doi: [10.1086/505038](https://doi.org/10.1086/505038)
- Saintonge, A., Catinella, B., Tacconi, L. J., et al. 2017, *ApJS*, 233, 22, doi: [10.3847/1538-4365/aa97e0](https://doi.org/10.3847/1538-4365/aa97e0)
- Salim, S., & Narayanan, D. 2020, *ARA&A*, 58, 529, doi: [10.1146/annurev-astro-032620-021933](https://doi.org/10.1146/annurev-astro-032620-021933)
- Salim, S., Lee, J. C., Janowiecki, S., et al. 2016, *ApJS*, 227, 2, doi: [10.3847/0067-0049/227/1/2](https://doi.org/10.3847/0067-0049/227/1/2)
- Sheth, K., Regan, M., Hinz, J. L., et al. 2010, *PASP*, 122, 1397, doi: [10.1086/657638](https://doi.org/10.1086/657638)
- Silva, L., Granato, G. L., Bressan, A., & Danese, L. 1998a, *ApJ*, 509, 103, doi: [10.1086/306476](https://doi.org/10.1086/306476)
- . 1998b, *ApJ*, 509, 103, doi: [10.1086/306476](https://doi.org/10.1086/306476)
- Skrutskie, M. F., Cutri, R. M., Stiening, R., et al. 2006, *AJ*, 131, 1163, doi: [10.1086/498708](https://doi.org/10.1086/498708)
- Spinoglio, L., Malkan, M. A., Rush, B., Carrasco, L., & Recillas-Cruz, E. 1995, *ApJ*, 453, 616, doi: [10.1086/176425](https://doi.org/10.1086/176425)
- Stern, D., Assef, R. J., Benford, D. J., et al. 2012, *ApJ*, 753, 30, doi: [10.1088/0004-637X/753/1/30](https://doi.org/10.1088/0004-637X/753/1/30)
- Sun, J., Leroy, A. K., Ostriker, E. C., et al. 2023, *ApJL*, 945, L19, doi: [10.3847/2041-8213/acbd9c](https://doi.org/10.3847/2041-8213/acbd9c)
- Takeuchi, T. T., Buat, V., Iglesias-Páramo, J., Boselli, A., & Burgarella, D. 2005, *A&A*, 432, 423, doi: [10.1051/0004-6361:20042189](https://doi.org/10.1051/0004-6361:20042189)
- Tully, R. B., Courtois, H. M., & Sorce, J. G. 2016, *The Astronomical Journal*, 152, 50, doi: [10.3847/0004-6256/152/2/50](https://doi.org/10.3847/0004-6256/152/2/50)
- van der Walt, S., Colbert, S. C., & Varoquaux, G. 2011, *Computing in Science and Engineering*, 13, 22, doi: [10.1109/MCSE.2011.37](https://doi.org/10.1109/MCSE.2011.37)
- Viaene, S., Baes, M., Tamm, A., et al. 2017, *A&A*, 599, A64, doi: [10.1051/0004-6361/201629251](https://doi.org/10.1051/0004-6361/201629251)
- Virtanen, P., Gommers, R., Oliphant, T. E., et al. 2020, *Nature Methods*, 17, 261, doi: [10.1038/s41592-019-0686-2](https://doi.org/10.1038/s41592-019-0686-2)
- Watkins, A. E., Salo, H., Laurikainen, E., et al. 2022, *A&A*, 660, A69, doi: [10.1051/0004-6361/202142627](https://doi.org/10.1051/0004-6361/202142627)
- Wetzell, A. R., Tinker, J. L., & Conroy, C. 2012, *MNRAS*, 424, 232, doi: [10.1111/j.1365-2966.2012.21188.x](https://doi.org/10.1111/j.1365-2966.2012.21188.x)
- Whitaker, K. E., Franx, M., Leja, J., et al. 2014, *ApJ*, 795, 104, doi: [10.1088/0004-637X/795/2/104](https://doi.org/10.1088/0004-637X/795/2/104)
- Williams, T. G., Baes, M., De Looze, I., et al. 2019, *MNRAS*, 487, 2753, doi: [10.1093/mnras/stz1441](https://doi.org/10.1093/mnras/stz1441)
- Wright, E. L., Eisenhardt, P. R. M., Mainzer, A. K., et al. 2010, *AJ*, 140, 1868, doi: [10.1088/0004-6256/140/6/1868](https://doi.org/10.1088/0004-6256/140/6/1868)
- Wyder, T. K., Martin, D. C., Schiminovich, D., et al. 2007, *ApJS*, 173, 293, doi: [10.1086/521402](https://doi.org/10.1086/521402)
- Yao, H. F. M., Jarrett, T. H., Cluver, M. E., et al. 2020, *ApJ*, 903, 91, doi: [10.3847/1538-4357/abba1a](https://doi.org/10.3847/1538-4357/abba1a)
- Zahid, H. J., Dima, G. I., Kewley, L. J., Erb, D. K., & Davé, R. 2012, *ApJ*, 757, 54, doi: [10.1088/0004-637X/757/1/54](https://doi.org/10.1088/0004-637X/757/1/54)

Zhang, L., & Ho, L. C. 2023, ApJ, 943, 60,  
doi: [10.3847/1538-4357/acab60](https://doi.org/10.3847/1538-4357/acab60)

**Table 1.** Measured WISE Properties of the S<sup>4</sup>G Sample

Name	R.A.	Dec.	W1	W1 flag	W2	W2 flag
	(deg)	(deg)	(mag)		(mag)	
IC5269	344.43176	-36.02611	9.402 ± 0.012	10	9.425 ± 0.015	10
IC5269A	343.98248	-36.34820	11.777 ± 0.015	10	11.738 ± 0.038	10
IC5269B	344.15277	-36.25002	10.056 ± 0.015	10	9.913 ± 0.023	10
IC5269C	345.20078	-35.37063	11.228 ± 0.013	10	11.230 ± 0.031	10
IC5270	344.47852	-35.85812	9.146 ± 0.011	10	8.995 ± 0.013	10
IC5271	344.50778	-33.74209	8.158 ± 0.011	10	8.107 ± 0.013	10
IC5273	344.8613	-37.70278	8.511 ± 0.012	10	8.465 ± 0.013	10
IC5321	351.5834	-17.95617	11.192 ± 0.013	10	11.062 ± 0.022	10
IC5325	352.18112	-41.33379	8.187 ± 0.011	10	8.113 ± 0.012	10
IC5332	353.61423	-36.10089	7.961 ± 0.015	10	7.910 ± 0.025	10

W3	W3 flag	W4	W4 flag	Radius <sup>a</sup>	b/a <sup>a</sup>	P.A. <sup>a</sup>
(mag)		(mag)		(arcsec)		(deg)
8.717 ± 0.080	10	7.987 ± 0.292	2	79.82	0.556	50.1
8.647 ± 0.087	10	7.065 ± 0.274	0	45.88	0.827	61.3
7.620 ± 0.055	10	5.908 ± 0.124	10	149.87	0.240	97.1
8.764 ± 0.109	10	6.588 ± 0.250	0	81.89	0.451	47.6
5.439 ± 0.017	10	3.630 ± 0.023	10	109.00	0.380	102.8
5.130 ± 0.017	10	3.346 ± 0.022	10	110.44	0.483	138.1
5.126 ± 0.022	10	3.048 ± 0.027	10	113.38	0.762	48.3
7.502 ± 0.033	10	5.304 ± 0.047	10	44.12	0.691	35.3
4.656 ± 0.017	10	2.883 ± 0.021	10	112.58	0.907	12.2
5.246 ± 0.059	10	3.571 ± 0.092	10	246.26	0.968	169.5

<sup>a</sup>Measured in the W1 band

NOTE—Table 1 is published in its entirety in the machine-readable format. A portion is shown here for guidance regarding its form and content.

A null value in the uncertainty of a quantity when the quantity is non-null indicates an upper limit value for the quantity.

The flag for each band indicates if the measurement was from: (0) isophotal aperture of semi-major axis "Radius," axis ratio, and position angle, or (10) the total flux combining the isophotal with the radial surface brightness extrapolation (see Jarrett et al. 2019), or (5) an isophotal aperture with an aperture correction (see Jarrett et al. 2023), or (2) the standard aperture measurement from the ALLWISE measurement, or (1) the point-source measurement from the ALLWISE catalog.

**Table 2.** Derived WISE Properties of the S<sup>4</sup>G Sample

Name	D <sub>lum</sub> (Mpc)	W1-W2 (mag)	W2-W3 (mag)	W1-W3 (mag)	W3-W4 (mag)
IC5269	27.37	-0.021 ± 0.035	0.529 ± 0.063	0.508 ± 0.063	0.788 ± 0.286
IC5269A	37.48	0.028 ± 0.051	2.864 ± 0.100	2.891 ± 0.093	1.898 ± 0.289
IC5269B	21.49	0.115 ± 0.041	2.368 ± 0.067	2.483 ± 0.065	1.563 ± 0.139
IC5269C	21.7	-0.009 ± 0.045	2.491 ± 0.117	2.482 ± 0.114	2.218 ± 0.274
IC5270	26.29	0.149 ± 0.035	3.547 ± 0.037	3.696 ± 0.037	1.836 ± 0.042
IC5271	25.59	0.05 ± 0.035	2.970 ± 0.037	3.020 ± 0.037	1.795 ± 0.041
IC5273	16.6	0.057 ± 0.035	3.316 ± 0.040	3.373 ± 0.040	2.058 ± 0.046
IC5321	43.22	0.110 ± 0.040	3.516 ± 0.050	3.626 ± 0.047	2.249 ± 0.065
IC5325	18.03	0.073 ± 0.035	3.450 ± 0.037	3.523 ± 0.037	1.793 ± 0.041
IC5332	6.18	0.076 ± 0.042	2.660 ± 0.071	2.736 ± 0.068	1.715 ± 0.113
IC5333	27.28	0.149 ± 0.036	3.326 ± 0.038	3.476 ± 0.037	1.958 ± 0.047

Log L <sub>W1</sub> (L <sub>⊙</sub> )	Log L <sub>W2</sub> (L <sub>⊙</sub> )	Log L <sub>W3</sub> <sup>a</sup> (L <sub>⊙</sub> )	Log L <sub>W4</sub> <sup>b</sup> (L <sub>⊙</sub> )	Log L <sub>W1Sun</sub> <sup>c</sup> (L <sub>⊙,W1</sub> )	Log M <sub>Stellar</sub> (M <sub>⊙</sub> )	SFR (M <sub>⊙</sub> /yr)
9.0392 ± 0.0099	8.6336 ± 0.0103	7.2903 ± 0.0347	6.5773 ± 0.1165	10.4013 ± 0.0139	10.035 ± 0.082	0.0241 ± 0.0059
8.3601 ± 0.0107	7.9785 ± 0.0178	8.005 ± 0.0365	7.8137 ± 0.1121	9.7231 ± 0.0145	9.298 ± 0.084	0.2764 ± 0.0730
8.5712 ± 0.0107	8.2312 ± 0.0128	7.8952 ± 0.0241	7.7841 ± 0.0511	9.9327 ± 0.0145	9.476 ± 0.083	0.2741 ± 0.0675
8.1113 ± 0.0103	7.7128 ± 0.0153	7.4509 ± 0.0451	7.5313 ± 0.1019	9.4728 ± 0.0142	9.079 ± 0.083	0.1386 ± 0.0359
9.1086 ± 0.0099	8.7727 ± 0.0103	9.0021 ± 0.0112	8.8880 ± 0.0129	10.4705 ± 0.0139	9.946 ± 0.082	1.0429 ± 0.2510
9.4808 ± 0.0099	9.1035 ± 0.0103	9.0819 ± 0.0112	8.9736 ± 0.0126	10.8427 ± 0.0139	10.406 ± 0.082	1.2351 ± 0.2984
8.9665 ± 0.0100	8.5886 ± 0.0103	8.7228 ± 0.0126	8.7223 ± 0.0141	10.3275 ± 0.0141	9.869 ± 0.082	0.6644 ± 0.1656
8.7168 ± 0.0103	8.3717 ± 0.0126	8.6041 ± 0.0161	8.6522 ± 0.0211	10.0805 ± 0.0142	9.579 ± 0.083	0.4485 ± 0.1117
9.1681 ± 0.0098	8.8012 ± 0.0100	8.9870 ± 0.0112	8.8582 ± 0.0123	10.5292 ± 0.0139	10.055 ± 0.082	0.9977 ± 0.2399
8.3334 ± 0.0107	7.9570 ± 0.0134	7.7888 ± 0.0255	7.6439 ± 0.0383	9.6934 ± 0.0145	9.249 ± 0.083	0.2350 ± 0.0571
8.6371 ± 0.0100	8.3013 ± 0.0105	8.4319 ± 0.0115	8.3970 ± 0.0151	9.9992 ± 0.0141	9.487 ± 0.082	0.3486 ± 0.0858

<sup>a</sup>W3 band spectral luminosity,  $\text{Log } \nu L_\nu(12\mu\text{m})$ , after subtraction of the stellar continuum

<sup>b</sup>W4 band spectral luminosity,  $\text{Log } \nu L_\nu(23\mu\text{m})$ , after subtraction of the stellar continuum

<sup>c</sup>W1 in-band luminosity

NOTE—Table 2 is published in its entirety in the machine-readable format. A portion is shown here for guidance regarding its form and content.

A null value in the uncertainty of a quantity when the quantity is non-null indicates an upper limit value for the quantity.

**Table 3.** Measured WISE Properties of the SINGS/KINGFISH Sample

Name	R.A.	Dec.	W1	W1 flag	W2	W2 flag
	(deg)	(deg)	(mag)		(mag)	
NGC0337	14.95818	-7.57715	8.755 ± 0.012	10	8.512 ± 0.020	10
NGC0584	22.83642	-6.86802	7.173 ± 0.012	10	7.262 ± 0.013	10
NGC0628	24.17394	15.78366	6.416 ± 0.012	10	6.298 ± 0.016	10
NGC0855	33.51487	27.87732	9.626 ± 0.015	10	9.563 ± 0.029	10
NGC0925	36.81964	33.57917	7.511 ± 0.015	10	7.452 ± 0.030	10
NGC1097	41.57904	-30.27462	5.995 ± 0.011	10	5.890 ± 0.012	10
NGC1266	49.00312	-2.42736	9.371 ± 0.012	10	9.077 ± 0.013	10
NGC1316	50.67380	-37.20796	5.058 ± 0.011	10	5.098 ± 0.014	10
NGC1377	54.16280	-20.90195	9.483 ± 0.013	10	8.142 ± 0.012	10
NGC1404	54.71632	-35.59413	6.565 ± 0.014	10	6.602 ± 0.016	10
IC0342	56.70144	68.09635	3.935 ± 0.013	10	3.880 ± 0.013	10

W3	W3 flag	W4	W4 flag	Radius <sup>a</sup>	b/a <sup>a</sup>	P.A. <sup>a</sup>
(mag)		(mag)		(arcsec)		(deg)
4.928 ± 0.017	10	2.551 ± 0.020	10	101.98	0.622	131.8
6.702 ± 0.046	10	5.813 ± 0.093	10	190.48	0.784	70.6
2.736 ± 0.015	10	0.943 ± 0.019	10	324.47	0.819	86.4
7.230 ± 0.059	10	5.043 ± 0.073	10	103.48	0.449	65.4
4.350 ± 0.034	10	2.266 ± 0.058	10	311.71	0.501	110.1
2.487 ± 0.012	10	0.152 ± 0.014	10	403.14	0.793	127.4
6.207 ± 0.018	10	2.562 ± 0.017	10	65.89	0.733	115.4
4.259 ± 0.037	10	3.176 ± 0.046	10	769.06	0.645	34.7
4.689 ± 0.014	10	1.704 ± 0.013	10	72.06	0.636	92.0
5.878 ± 0.074	10	5.145 ± 0.067	10	251.23	0.880	160.0
0.225 ± 0.034	10	-1.815 ± 0.012	10	778.51	0.946	75.5

<sup>a</sup>Measured in the W1 band

NOTE—Table 3 is published in its entirety in the machine-readable format. A portion is shown here for guidance regarding its form and content. A null value in the uncertainty of a quantity when the quantity is non-null indicates an upper limit value for the quantity.

The flag for each band indicates if the measurement was from: (0) isophotal aperture of semi-major axis "Radius," axis ratio, and position angle, or (10) the total flux combining the isophotal with the radial surface brightness extrapolation (see Jarrett et al. 2019), or (5) an isophotal aperture with an aperture correction (see Jarrett et al. 2023), or (2) the standard aperture measurement from the ALLWISE measurement, or (1) the point-source measurement from the ALLWISE catalog.

**Table 4.** Derived WISE Properties of the SINGS/KINGFISH Sample

Name	D <sub>lum</sub> (Mpc)	W1-W2 (mag)	W2-W3 (mag)	W1-W3 (mag)	W3-W4 (mag)
NGC0337	20.62	0.231 ± 0.038	3.586 ± 0.040	3.816 ± 0.037	2.369 ± 0.040
NGC0584	21.53	-0.058 ± 0.035	0.359 ± 0.057	0.301 ± 0.056	0.975 ± 0.108
NGC0628	10.05	0.069 ± 0.034	3.668 ± 0.036	3.737 ± 0.035	1.797 ± 0.037
NGC0855	9.93	0.057 ± 0.044	2.382 ± 0.072	2.439 ± 0.068	2.166 ± 0.098
NGC0925	10.14	0.004 ± 0.035	3.259 ± 0.043	3.263 ± 0.042	1.910 ± 0.072
NGC1097	16.91	0.103 ± 0.035	3.408 ± 0.035	3.510 ± 0.035	2.345 ± 0.036
NGC1266	28.67	0.297 ± 0.035	2.871 ± 0.038	3.169 ± 0.037	3.660 ± 0.039
NGC1316	20.88	-0.026 ± 0.035	0.657 ± 0.050	0.630 ± 0.049	1.259 ± 0.066
NGC1377	23.99	1.362 ± 0.035	3.434 ± 0.036	4.796 ± 0.036	2.990 ± 0.036
NGC1404	20.15	-0.047 ± 0.037	0.468 ± 0.082	0.420 ± 0.081	0.965 ± 0.104
IC0342	3.65	0.080 ± 0.033	3.668 ± 0.045	3.748 ± 0.045	2.040 ± 0.045

Log L <sub>W1</sub> (L <sub>⊙</sub> )	Log L <sub>W2</sub> (L <sub>⊙</sub> )	Log L <sub>W3</sub> <sup>a</sup> (L <sub>⊙</sub> )	Log L <sub>W4</sub> <sup>b</sup> (L <sub>⊙</sub> )	Log L <sub>W1<sub>Sun</sub></sub> <sup>c</sup> (L <sub>⊙,w1</sub> )	Log M <sub>Stellar</sub> (M <sub>⊙</sub> )	SFR (M <sub>⊙</sub> /yr)
9.0612 ± 0.0099	8.7620 ± 0.0119	9.0033 ± 0.0111	9.1125 ± 0.0120	10.4226 ± 0.0140	9.849 ± 0.082	0.9720 ± 0.2349
9.7284 ± 0.0100	9.2946 ± 0.0102	4.5717 ± ...	7.3612 ± 0.0437	11.0898 ± 0.0140	10.749 ± 0.082	0.0431 ± 0.0151
9.3512 ± 0.0098	8.9836 ± 0.0100	9.2535 ± 0.0104	9.1243 ± 0.0109	10.7115 ± 0.0139	10.229 ± 0.082	1.7232 ± 0.4193
8.0809 ± 0.0106	7.7077 ± 0.0146	7.3828 ± 0.0254	7.4705 ± 0.0309	9.4412 ± 0.0145	9.014 ± 0.083	0.0683 ± 0.0163
8.9029 ± 0.0097	8.5073 ± 0.0102	8.6025 ± 0.014	8.5813 ± 0.0258	10.2632 ± 0.0139	9.840 ± 0.082	0.7979 ± 0.1986
9.9905 ± 0.0098	9.6350 ± 0.0100	9.7998 ± 0.0101	9.8988 ± 0.0105	11.3515 ± 0.0139	10.873 ± 0.082	5.3952 ± 1.4339
9.0969 ± 0.0099	8.8174 ± 0.0102	8.7617 ± 0.0114	9.3985 ± 0.0112	10.4591 ± 0.0140	9.899 ± 0.082	1.0374 ± 0.2615
10.5457 ± 0.0099	10.1314 ± 0.0105	8.5900 ± 0.0443	8.6443 ± 0.0218	11.9071 ± 0.0139	11.566 ± 0.082	0.3990 ± 0.0969
8.9018 ± 0.0102	9.0442 ± 0.0101	9.2442 ± 0.0105	9.5874 ± 0.0103	10.2635 ± 0.0142	9.444 ± 0.083	1.9715 ± 0.4837
9.9121 ± 0.0105	9.4988 ± 0.0109	7.6461 ± 0.0938	7.6236 ± 0.0336	11.2734 ± 0.0144	10.929 ± 0.082	0.0708 ± 0.0178
9.5224 ± 0.0094	9.1360 ± 0.0097	9.4044 ± 0.0154	9.3533 ± 0.0100	10.8821 ± 0.0137	10.394 ± 0.082	2.5307 ± 0.6219

<sup>a</sup>W3 band spectral luminosity,  $\text{Log } \nu L_\nu(12\mu\text{m})$ , after subtraction of the stellar continuum

<sup>b</sup>W4 band spectral luminosity,  $\text{Log } \nu L_\nu(23\mu\text{m})$ , after subtraction of the stellar continuum

<sup>c</sup>W1 in-band luminosity

NOTE—Table 4 is published in its entirety in the machine-readable format. A portion is shown here for guidance regarding its form and content.

A null value in the uncertainty of a quantity when the quantity is non-null indicates an upper limit value for the quantity.